Metabolic Immunomodulation, Transcriptional Regulation, and Signal Protein Expression Define the Metabotype and Effector Functions of Five Polarized Macrophage Phenotypes

Catherine B. Anders Ph.D.*, Tyler M.W. Lawton*, Hannah Smith*†, Jamie Garret*‡, and Mary Cloud B. Ammons Ph.D.*

* Idaho Veteran's Research and Education Foundation (IVREF); Boise VA Medical Center (BVAMC), Boise, ID 83702; USA

† Department of Microbiology and Immunology; Montana State University, Bozeman, MT, ZIP 59717; USA

‡ School of Medicine, University of Washington, Seattle, WA, ZIP 98195; USA

Corresponding Author

Summary Sentence

Key Words: Macrophage, Immunomodulation, Metabolism, Plasticity

Abbreviations

AHS	autologous human serum
APCs	antigen-presenting cells
ATP	adenosine triphosphate
bFGF	basic fibroblast growth factor
BSA	bovine serum albumin
CD	cluster of differentiation
DAMPs	damage-associated molecular patterns
DGS	directed global significance
ECM	extra cellular matrix
EGF	epidermal growth factor
FAO	fatty acid oxidation
FAs	fatty acids
FGF	fibroblast growth factor
FMO	fluorescence minus one
GM-CSF	granulocyte-macrophage colony-stimulating factor
GO	gene ontology
GSEA	Gene set enrichment analysis
HC	hierarchical clustering
HESI-II	heated electrospray ionization
HIF	hypoxia-inducible factor
HIF	hypoxia-inducible factor
HLA-DR	human leukocyte antigen – DR isotype
ICs	immune complexes
IFN-γ	interferon gamma
IL	interleukin
IL-1ra	IL-1 receptor agonist
IRB	institutional review board
LIF	leukemia inhibitory factor
LPS	lipopolysaccharides
M-CSF	macrophage colony stimulating factor
MEM	minimum essential media
MerTK	Mer receptor tyrosine kinase
MFI	median fluorescence intensity
MHC-II	major histocompatibility complex class II
MMP	matrix metalloproteases
MΦs	macrophages
NADPH	nicotinamide adenine dinucleotide phosphate
NO	nitric oxide
NO	nitric oxide
OPLSDA	orthogonal PLSDA
OXPHOS	oxidative phosphorylation
PBMCs	primary blood-derived mononuclear cells

PBS	phosphate buffered saline
PCA	principal component analysis
PDGF	platelet-derived growth factor
PFPA	perfluoropentanoic acid
PGF	placental growth factor
PLSDA	partial least-squares to latent structures discriminant analysis
PPP	pentose phosphate pathway
QC	quality control
RNS	reactive nitrogen species
ROS	reactive oxygen species
RPMI	Roswell Park Memorial Institute
RSD	relative standard deviation
SDEGs	significantly differentially expressed genes
SDH	succinate dehydrogenase
SDH	succinate dehydrogenase
SPMs	specialized pro-resolving mediators
SUS	Shared and Unique Structure
TAMs	Tumor-associated MΦs
TCA	tricarboxylic acid cycle
TGF-β	transforming growth factor-β
TLR	Toll-like receptor
TNF	tumor necrosis factor
TXN	thioredoxin
UDS	undirected global significance
UHPLC/MS/MS	ultra-high-performance liquid chromatography/tandem accurate mass spectrometry
VEGF	vascular endothelial growth factor

Abstract

As of 2013, there were nearly 30 million Americans with diabetes or one in ten adults, but by 2050, estimates from the American Diabetes Association indicate that one in three adults (~350 million Americans) will be diabetic. At current rates of amputation (~25%) due to non-healing wounds, this 2050 population will have to absorb the social and economic burden of over 85 million diabetic amputees. While normal wound healing proceeds through a well-described iterative process, in non-healing wounds this process stalls at the transition from inflammation to tissue repair. Our central hypothesis is that macrophage plasticity is key to this transition and directly facilitates shifting the wound environment from pro-inflammatory to promoting tissue repair. While more established signaling molecules of immunity (such as cytokines and chemokines) remain essential to

driving functional phenotype in the immune system, recent advances in metabolomics profiling have revealed a pivotal role for metabolites in immunomodulation. Presented herein, an ex vivo macrophage culture model produces five macrophage functional phenotypes compared to the parent resting macrophage phenotype and is a systems-level model for understanding the contribution of metabolism to macrophage functional plasticity. Specifically, CD14+ peripheral blood monocytes are isolated, differentiated into M0 macrophages, and polarized into the M1 (IFN-gamma;/LPS), M2a (IL-4/IL-13), M2b (IC/LPS), M2c (IL-10), and M2d (IL-6/LIF) phenotypes. Each phenotype is then characterized by a bioanalyte matrix of four cell surface markers, ~50 secreted immunomodulating proteins (cytokines, chemokines, and growth factors), ~800 myeloid genes, and ~450 identified metabolites (including lipids). Signal protein profiles and pathway enrichment analysis of expressed genes generally groups the phenotypes into pro-inflammatory (M1 and M2b) and tissue repair/regenerative (M2a, M2c, and M2d); however, clear distinctions between each phenotype can be made. For example, M1 macrophages activate processes that facilitate acute inflammatory responses through control of nitric oxide (NO) and reactive oxygen species (ROS), whereas M2b macrophages activate processes that regulate chronic inflammation and chemotaxis of lymphocytes, endothelial cells, and epithelial cells. Furthermore, both M2c and M2d macrophages activate angiogenesis processes, but M2c macrophages promote extracellular matrix (ECM) assembly while M2d macrophages activate processes that drive ECM degradation. Finally, metabolomics profiles further validate recent findings that shifts between aerobic glycolysis, the pentose phosphate pathway, and oxidative phosphorylation distinguish pro-inflammatory macrophages and tissue repair/regeneration macrophages; however, our model provides further evidence to support the association between metabolism (such as decoupling of the TCA cycle, fatty acid synthesis, and -oxidation) and functional phenotype. Metabolomics is fundamentally changing our understanding of immunomodulation in diverse macrophage populations and that deeper understanding is informing our long-term goals of developing novel diagnostic and therapeutic approaches to wound healing. By integrating metabolomics into our systematic characterization of these phenotypes, we have developed quantifiable metrics that not only define metabolic and functional phenotype, but also provide insight into the cellular functions fundamental to macrophage plasticity.

Introduction

Macrophages (MΦs) display remarkable functional plasticity and the ability to activate diverse responses to a host of intracellular triggers, external stimuli, and nutritional availability. Generally, MΦs are divided into M1(classically activated, pro-inflammatory) MΦs and a broad set of M2 (alternatively activated, anti-inflammatory) MΦs. M2 MΦs have been further subdivided into M2a, M2b, M2c, and M2d subtypes [1, 2]. These M2 subtypes have been shown to demonstrate numerous, often overlapping, effector functions [3-8], and have emerged as keystone species in the functional ecology of such diverse environments as wounds [9], tumors [10-12], developing fetuses [13], and systemic autoimmune diseases [14-16]. Comprehensive, functional characterization of such a diverse array of MΦ populations presents an immense challenge and requires utilization of a systems-based approach that integrates transcriptional, proteomic, and metabolomic profiles to fully characterize these diverse MΦ functional phenotypes. The emergent field of metabolomics has established a pivotal role for metabolism in immunomodulation of MΦ politization and functional phenotypes (reviewed in O-Neill, et al. [17]); however, this research has been mainly limited to comparing the more established M1 and M2a phenotypes, leaving much to be learned about the other known M2 MΦ subtypes (i.e. M2b, M2c, and M2d).

Classically activated, pro-inflammatory M1 MΦs are polarized by exposure to interferon gamma (IFN-γ), tumor necrosis factor (TNF), lipopolysaccharides (LPS), and/or other antimicrobial signals that trigger Toll-like receptor (TLR) ligation [18]. M1 MΦs exhibit increased and sustained pro-inflammatory responses including production of such anti-microbial molecules as reactive nitrogen species (RNS) and reactive oxygen species (ROS), secretion of inflammatory mediators such as interleukin-6 (IL-6), IL-1β, IL-12, IL-18, and TNFα [19]. The upregulation of major histocompatibility complex class II (MHC-II) and T-cell priming surface markers (e.g. cluster of differentiation (CD)40, CD80, and CD86), as well as chemokine production (e.g. CXCL9, CXCL10, and CXCL11) in M1 MΦs promote Type I immunity through the Th1 and Th17 cytotoxic adaptive

immune responses [19-21]. Although essential for defense against infection, continuous M1 polarization of MΦs can lead to impaired wound healing and significant collateral tissue damage from sustained inflammation. Phagocytosis of apoptotic cells, detection of damage-associated molecular patterns (DAMPs or alarmins), and production of IL-5, IL-4, and IL-13 by nearby cells dampens M1-driven inflammation and facilitates the onset of an anti-inflammatory, tissue repair response dominated by M2 MΦ functional phenotypes [22-24].

M2 MΦs (M2a, M2b, M2c, and M2d) having been described as representing the opposite end of the polarization spectrum from M1 MΦs, exhibit tissue-reparative, pro-fibrotic, pro-angiogenic, and phagocytic functions [1, 25-27]. Associated with Type 2 immunity and helper T-cell priming, M2 MΦs are proposed to counteract the inflammatory microenvironment created by the M1 MΦ phenotype [28, 29]. M2a MΦs, polarized by exposure to IL-4 and IL-13, have been described as expressing high levels of MHC-II, mannose receptor (CD206), transmembrane fatty acid translocase (CD36), and secreting IL-1 receptor agonist (IL-1ra) to promote helper T-cell activation and suppress IL-1 mediated inflammation [1, 25, 28]. Additionally, M2 MΦs have been shown to secrete chemokines, fibronectins, and growth factors (e.g. fibroblast growth factor [FGF] and transforming growth factor-β [TGF-β]) to initiate cellular proliferation, recruit tissue-repair cellular populations, promote angiogenesis, and support development of myofibroblasts [23, 30, 31].

M2b MΦs, polarized by exposure to LPS and immune complexes (ICs), have been shown to crosslink Fcγ receptors via ICs, inducing elevated CD80/CD86 expression for T-cell priming, high IL-10 secretion, low IL-12 secretion, and promotion of Type 2 immunity [25, 32-34]. M2b MΦs, observed to be ineffective at bacterial clearance [35], display characteristics indicative of a tissue remodeling functional phenotype including extra cellular matrix (ECM) synthesis and angiogenic potential [36].

Resting MΦ exposure to IL-10, glucocorticoids, or TGFβ, drives MΦ polarization towards the M2c phenotype, and has been characterized as having increased expression of the Mer receptor tyrosine kinase (MerTK), surface display of pathogen-sensing growth factor receptor (CD163), secretion of placental growth factor (PGF), and activation of metalloproteinases (MMPs). Based on this profile, M2c MΦs are proposed to promote tissue repair

through efferocytosis, ECM remodeling, and angiogenesis [26, 37]. While this phenotype appears to overlap with the M2a MΦ functional phenotype, Gabriel, et al. [38] demonstrated differences in the timing of gene expression during polarization and proposed that this temporal polarization may distinguish these MΦ phenotypes *in vivo*. Additionally, Jetten, et al. [30] showed that while PGF signaling was necessary for M2c MΦ-induced angiogenesis, PGF was not required for angiogenesis promoted by M2a MΦs.

Tumor-associated MΦs (TAMs, referred to herein as M2d MΦs), previously investigated within the tumor microenvironment, can be polarized through a variety of mechanisms including co-culture with cancer cells or ascites fluid, exposure to IL-6, leukemia inhibitory factor (LIF), and/or the purine nucleoside adenosine [27, 39]. M2d MΦs are associated with potent immunosuppressive functions and the promotion of angiogenesis [27]. M2d MΦs have also been shown to secrete numerous proteolytic enzymes (e.g. matrix metalloproteases (MMP)-2, MMP-9, and cathepsins), growth factors ((e.g. epidermal growth factor (EGF), vascular endothelial growth factor (VEGF), platelet-derived growth factor (PDGF) and basic FGF (bFGF)), and anti-inflammatory mediators (e.g. IL-10, TGF-β, B7-H1, B7-H3/H4). While clear functional overlap with other M2 MΦs exists, the role of M2d MΦs within the healing wound remains unknown.

While MΦ functionality remains to be comprehensively described for each of these phenotypes, M1/M2a MΦ plasticity has been demonstrated to depend on metabolic immunomodulation [17]. M1 MΦ polarization favors aerobic glycolysis and glycolytic flux into the oxidative branch of the pentose phosphate pathway (PPP), generating nicotinamide adenine dinucleotide phosphate (NADPH) to feed the oxidative burst and serve as the building block for rapid biosynthesis (reviewed in Artyomov, 2016) [40]. Activation of PPP also supports the production of glutathione and other antioxidants to promote cellular longevity under the harsh conditions created by this pro-inflammatory MΦ phenotype [41]. This anti-microbial function is further enhanced by a decoupled anaplerotic tricarboxylic acid cycle (TCA) with breaks at citrate and succinate. Accumulated citrate from the broken TCA cycle is diverted for the biosynthesis of fatty acids (FAs), prostaglandins, the anti-microbial metabolite itaconate, and the generation of nitric oxide (NO) [41-43]. Elevated itaconate inhibits

succinate dehydrogenase (SDH), resulting in succinate accumulation, hypoxia-inducible factor (HIF) stabilization, and HIF-mediated expression of pro-inflammatory cytokines [41, 44, 45].

In contrast, M2a MΦs utilize glycolysis to feed an intact TCA cycle coupled with FA oxidation (FAO), and active oxidative phosphorylation (OXPHOS) to generate adenosine triphosphate (ATP. FAO also plays a role in reducing inflammation through reduced lipid accumulation and inhibition of pro-inflammatory mediators [46, 47]. Additionally, M2a MΦs rely heavily on glutamine to promote the hexosamine pathway needed the for production of N-glycans and the upregulation of the mannose receptor [42]. Finally, arginine flux through ornithine contributes to collagen production and polyamine synthesis [42, 48].

Much less is known regarding metabolic immunomodulation of the remaining M2 MΦ phenotypes (M2b, M2c, and M2d). Rodriguez-Prados, et al. (2010) [44] demonstrated that, like M1 and M2a MΦs, M2c MΦs utilize glycolysis; however, only M1 MΦs consumed glucose to produce lactate, indicating M1 MΦ use of aerobic glycolysis is unique and both M2a and M2c MΦs utilize glycolysis to drive an intact TCA. In contrast, M2a and M2c MΦs could be distinguished based on glutamine consumption, suggesting a metabolic contribution to the unique mannose expression on M2a MΦs (REF). Elevated glycolysis has also been demonstrated in M2d MΦs, but as a means to promote angiogenesis and tumor metastasis [10]. Like M1 MΦs, M2b cells have been shown to generate NO combined with decreased production of urea [25]. Overall, alternately activated M2 MΦs have been demonstrated to have an intact TCA, increased OXPHOS, low cellular energy (e.g. high AMP/ATP ratios), and elevated catabolism of FAs [49]; however, inconsistent metabolic profiles reported for murine-derived MΦs when compared to human-derived MΦs demonstrates how much is still unknown about how metabolism drives function in these diverse MΦ phenotypes [50, 51].

Although multiple MΦ functional phenotypes have been described in the literature (reviewed in Anders, et. al. 2019), key components of metabolic immunomodulation driving this functional diversity remain to be comprehensively elucidated. To address this knowledge gap, we utilized a systems biology approach to comprehensively examine an *ex vivo* MΦ model that produced six functional phenotypes. Briefly, CD14+

PBMCs isolated from healthy human donors were differentiated into resting MΦs (referred to as M0 MΦs). MΦ subsets were then polarized into M1 (IFN-γ/LPS), M2a (IL-4/IL-13), M2b (IC/LPS), M2c (IL-10), and M2d (IL-6/LIF) MΦ phenotypes. The MΦs were then profiled using a bioanalyte matrix consisting of four cell surface markers, ~50 secreted cytokines/chemokines/growth-factors, ~800 expressed myeloid genes and ~450 identified metabolites. By integrating metabolomics into a systems analysis of MΦ phenotypes, we provide the most comprehensive map of MΦ diversity to date, as well as the global metabolic shifts driving MΦ functional plasticity in these phenotypes.

Materials and Methods

Human Subjects, Monocyte Isolation, and Macrophage Differentiation and Polarization

Written informed consent was obtained from healthy human subjects (ages 18-60 years old) enrolled in the study approved by the VA Puget Sound institutional review board (IRB). Whole blood (100 mL total) was obtained through venipuncture. 70 mL of blood was drawn into 60-mL syringe tubes pretreated with heparin (Fresenius Kabi USA, LLC; Lake Zurich, Illinois, USA) while 30 mL was collected into BD Vacutainer Serum tubes (Franklin Lakes, NJ). The vacutainer serum tubes were incubated at room temperature for 30-60 minutes before centrifugation at 3500 rpm for 20 minutes. The separated serum was collected and stored at -20° C. Primary blood-derived mononuclear cells (PBMCs) were obtained via Ficoll-paque density centrifugation (Ficoll-Paque Plus, GE Healthcare Bio-Sciences; Uppsala, Sweden) followed by CD14+ monocyte isolation via negative immunomagnetic selection using the Pan Monocyte Isolation Kit (Miltenyi Biotech; Bergisch Gladbach, Germany). Monocytes were cultured in Roswell Park Memorial Institute (RPMI) 1640 (Corning; Manassa, VA, USA) modified with 1% (v/v) each of minimum essential media (MEM) non-essential amino acids (Gibco; Grand Island, NY, USA), sodium pyruvate (Gibco; Grand Island, NY, USA) and L-glutamine (Lonza; Walkersville, MD, USA) at a cellular density of 1.5 x 10^6 cells/mL in 6-well cell culture plates. Additionally, this media was supplemented with 10% (v/v) autologous human serum (AHS) that was pooled from a minimum of four healthy human donors and 50 ng/mL of recombinant human MΦ colony-stimulating

factor (M-CSF) (Biolegend; San Diego, CA, USA). All cellular cultures were incubated at 37° C with 5% CO_2. On day 4, the media was replaced with the modified RPMI 1640 supplemented with 10 % pooled AHS and 50 ng/mL of recombinant human MΦ colony stimulating factor (M-CSF). On day 7, the media was replaced as described above and treated with predefined polarization stimuli to achieve the desired MΦ phenotype. Cells exposed to M-CSF alone produce an M0 phenotype. To achieve the classically activated M1 phenotype the cells were exposed to 100 ng/mL LPS from Escherichia coli O111:B4 (Sigma Aldrich; St. Louis, MO, USA) and 20 ng/mL recombinant human IFN-γ (PeproTech; Rock Hill, NJ, USA). Alternately activated MΦs traditionally designated as M2a, M2b, M2c, and M2d MΦs resulted from stimulation with 20 ng/mL recombinant human interleukin (IL) -4 (IL-4; PeproTech; Rock Hill, NJ, USA) and 25 ng/mL recombinant human IL-13 (PeproTech; Rock Hill, NJ, USA) for the M2a phenotype, 100 ng/mL LPS and 16.7 µL/mL immune complexes (IC; see details below) resulted in M2b cells, 25 ng/mL recombinant human IL-10 (PeproTech; Rock Hill, NJ, USA) for the M2c phenotype, and 50 ng/mL recombinant human IL-6 (R&D Systems; Minneapolis, MN, USA) and 25 ng/mL recombinant human Leukemia inhibitory factor (LIF; R&D Systems; Minneapolis, MN, USA) to achieve the M2d phenotype. Immune complexes (IC) for M2b polarization were created by mixing 1 µL of a 1.32 mg/mL solution of bovine serum albumin (BSA; MP Biomedicals; Auckland, New Zealand) with 50 µL anti-albumin (bovine serum), rabbit IgG fraction polyclonal antibodies (Invitrogen; Eugene, OR) and incubated at 37° C for one hour. This IC mixture can then be stored at 4 degrees Celsius until needed (i.e. such as overnight). The polarized cells were incubated at 37° C with 5% CO_2 for 24 – 72 hours depending on the desired downstream experimentation.

Characterization of MΦ Phenotypes

Flow Cytometry Analysis

Flow cytometry was conducted to access differences in cell surface marker expression between the six different phenotypes. Preliminary experiments were conducted using CD 14+ monocytes on Days 2, 5 and 7 post-plating to differentiate between monocytes, immature MΦs, and mature M0 MΦs and identify gating regions for future

MΦ phenotype experiments. For MΦ phenotype experiments, a panel of four fluorescent markers was employed including FITC mouse anti-human CD40 (BD Biosciences; San Jose, CA, USA), PE mouse anti-human CD86 (BD Biosciences; San Jose, CA, USA), PerCP-Cy™5.5 mouse anti-human CD163 (BD Biosciences; San Jose, CA, USA) and APC mouse anti-human HLA-DR (BD Biosciences; San Jose, CA, USA). Unstained cells, single stained cells, and fluorescent minus one (FMO) controls were included for each analyzed phenotype to identify unstained cellular populations. All samples were evaluated on an Accuri C6 flow cytometer (BD Biosciences; San Jose, CA, USA) and the data analyzed using Kaluza 2.1 Analysis software (Beckman Coulter; Indianapolis, Indiana, USA).

Intracellular Metabolite Isolation and Analysis

To obtain a comprehensive snapshot of cellular function, multiple experimental sample types were collected from each MΦ phenotype during cell harvest. This approach allowed for the collection of transcriptomic, proteomic, and metabolomic data from each experimental trial. At the desired time point, the cellular supernatant, comprised of cell culture media and any non-adherent cells, was removed from the cell culture and placed into falcon tubes on ice. One mL of ice-cold phosphate buffered saline (PBS) was added to the adherent cell layers and then removed to the tubes containing the cellular supernatant and the tubes centrifuged at 2000 rpm for 8 minutes. The collected supernatant and stored at -80° C until further analysis. The remaining cell pellets were flash-frozen in liquid nitrogen and placed on ice. The adherent cells were quenched with 350 µL of 100% methanol (Honeywell; Muskegon, MI, USA) cooled to -80° C followed by 350 µL of ice-cold Ultrapure distilled water (Invitrogen; Grand Island NY, USA) and the plates put on ice. The quenched cells were removed through gentle cell scraping and added to any cells collected in the initial step. 700 µL of chloroform (Acros Organics; Thermo Fisher Scientific; Waltham, MA, USA) at -20° C was then added to the collected cells and the tubes vortexed for 30 seconds. The contents of the tubes were transferred to FastPrep® lysing matrix D tubes (MP Biomedicals; Auckland, New Zealand); followed by cellular disruption utilizing the FastPrep-24™ 5G Homogenizer (MP Biomedicals; Auckland, New Zealand). To achieve cell lysis, the tubes were

homogenized during two cycles of 40 s each at 4.0 m/s with a 90 s delay between cycles. The homogenized samples were centrifuged at 16,000 xg for 5 minutes at 4° C. and then placed immediately on ice. The polar (methanol/water) layer and non-polar (chloroform) layers were subsequently transferred to 1.5 mL protein low binding microcentrifuge tubes. These metabolite suspensions were lyophilized overnight without heat on a Thermo Scientific™ Savant™ ISS110 SpeedVac™ (Waltham, MA, USA) and the lyophilized pellets stored at -80°C until the samples were shipped to Metabolon for further analysis. The remaining interphase layer was flash-frozen in liquid nitrogen and stored at -80°C until RNA extraction.

Metabolite Analysis

All samples were analyzed by Metabolon (Morrisville, NC, USA) using four ultra-high-performance liquid chromatography/tandem accurate mass spectrometry (UHPLC/MS/MS) methods. The following is a summary of Metabolon's procedure. All methods utilized a Waters ACQUITY ultra-performance liquid chromatography (UPLC) and a Thermo Scientific Q-Exactive high resolution/accurate mass spectrometer interfaced with a heated electrospray ionization (HESI-II) source and Orbitrap mass analyzer operated at 35,000 mass resolution. Lyophilized samples were reconstituted in solvents compatible to each of the four methods. Each reconstitution sample contained a series of standards at fixed concentrations to ensure injection and chromatographic consistency. One aliquot was analyzed using acidic positive ion conditions, chromatographically optimized for more hydrophilic compounds. In this method, the extract was gradient eluted from a C18 column (Waters UPLC BEH C18-2.1x100 mm, 1.7 µm) using water and methanol, containing 0.05% perfluoropentanoic acid (PFPA) and 0.1% formic acid. Another aliquot was also analyzed using acidic positive ion conditions that was chromatographically optimized for more hydrophobic compounds. In this method, the extract was gradient eluted from the same afore mentioned C18 column using methanol, acetonitrile, water, 0.05% PFPA and 0.01% formic acid and was operated at an overall higher organic content. Another aliquot was analyzed using basic negative ion optimized conditions using a separate dedicated C18 column. The basic extracts were gradient eluted from the column using methanol and water, however with 6.5mM Ammonium Bicarbonate at pH 8. The

fourth aliquot was analyzed via negative ionization following elution from a HILIC column (Waters UPLC BEH Amide 2.1x150 mm, 1.7 µm) using a gradient consisting of water and acetonitrile with 10mM Ammonium Formate, pH 10.8. The MS analysis alternated between MS and data-dependent MS scans using dynamic exclusion. The scan range varied slighted between methods but covered 70-1000 m/z. Several types of controls were analyzed in concert with the experimental samples: a pooled matrix sample generated by taking a small volume of each experimental sample served as a technical replicate throughout the data set; extracted water samples served as process blanks; and a cocktail of quality control (QC) standards that were carefully chosen not to interfere with the measurement of endogenous compounds were spiked into every analyzed sample, allowed instrument performance monitoring and aided chromatographic alignment. Instrument variability was determined by calculating the median relative standard deviation (RSD) for the standards that were added to each sample prior to injection into the mass spectrometers. Overall process variability was determined by calculating the median RSD for all endogenous metabolites (i.e., non-instrument standards) present in 100% of the pooled matrix samples. Experimental samples were randomized across the platform run with QC samples spaced evenly among the injections.

Raw data was extracted, peak-identified and QC processed using Metabolon's hardware and software. Compounds were identified by comparison to library entries of purified standards or recurrent unknown entities. Biochemical identifications are based on three criteria: retention index within a narrow RI window of the proposed identification, accurate mass match to the library +/- 10 ppm, and the MS/MS forward and reverse scores between the experimental data and authentic standards. The MS/MS scores are based on a comparison of the ions present in the experimental spectrum to the ions present in the library spectrum. Peaks were quantified using area-under-the-curve. The resulting data was then normalized to cell count to account for differences in metabolite levels due to differences in the amount of material present in each sample.

Metabolomics Data Analysis

After normalization, peak intensity values were uploaded into MetaboAnalyst 4.0 (Ste. Anne de Bellevue,

Quebec) [52], normalized using pareto scaling, and then statistically analyzed. Using MetaboAnalyst 4.0, partial least-squares to latent structures discriminant analysis (PLSDA) and orthogonal PLSDA (OPLSDA) were employed to characterize and visual metabolomic differences between the resting MO MΦs and the individually polarized phenotypes. For detailed descriptions of OPLSDA utilization with metabolomics data, readers are referred to Wiklund, et al., (2008) [53]. PLSDA, a regression method, was employed to identify relationships between the UHPLC/MS/MS data (X) and binary vectors (Y) with a value of 0 for M0 resting MΦs and 1 representing the polarized phenotype as they are compared individually to the M0 cells. Orthogonal PLS (OPLS) was then used to separate the systematic variation in X into two components. The first component, the predictive component (covariance), is linearly associated with Y and describes between phenotype variance. The second component (correlation) is orthogonal to Y and describes between sample variation [53].

To adequately demonstrate the OPLSDA results, three data visualization methods were utilized. The first, cross-validated score plots (insets Figure 5), display the cross-validated score values (Orthogonal T-score) on the y-axis versus the predictive or model T-score (T-score) on the x-axis for each sample point within the analysis. S-Plots were used to visualize the predictive component of the model. The x-axis represents the magnitude or covariance of each metabolite to the model while the reliability or correlation of those metabolites is plotted on the y-axis. Generally, metabolites that have covariance scores greater than 0.2 or less than -0.2. and correlation values greater than 0.6 or less than -0.6 are considered to contribute significantly to the predictive value of the model. Shared and Unique Structure (SUS) plots were employed to compare the results from two separate OPLS models. In the experiment, the M1 OPLS model was compared to each M2 (M2a, M2b, M2c and, M2d) phenotype model. The correlation scores for each M2 subtype was plotted on the y-axis and the M1 scores on the x-axis. In this representation, metabolite features that are shared between phenotypes will cluster close to the diagonals while those features unique to each phenotype will fall outside of the diagonals.

Cytokines, Chemokines and Growth Factors

All measured cytokines, chemokines and growth factors were measured using the supernatant collected during the intracellular metabolite extraction at 24- and 72-hr post polarization. The analytes were evaluated utilizing multiplex magnetic bead-based immunoassays (ProcartaPlex™, Thermo Fisher Scientific; Waltham, MA, USA) per the manufacturer's instructions, and were run on a MAGPIX® instrument (Luminex Corporation; Austin, TX, USA).

RNA Extraction

RNA was purified utilizing the Qiagen RNAeasy® plus mini kit (Germantown, MD, USA). The lysing tubes containing the interphase layer from the metabolite were first thawed on ice if needed. The interphase layer was then resuspended in the RLT lysis buffer supplemented with 1% (v/v) of β-mercaptoethanol followed by homogenization utilizing identical settings as described above. Following lysis, the RNA was extracted and purified according to the manufacturer's instructions. The integrity of the extracted RNA was evaluated on an Agilent 2200 Tape Station (Santa Clara, CA, USA). The RNA was diluted to a concentration of 20 ng/µL for a total concentration of 100 ng in 5 µL.

Nanostring analysis

The nCounter Gene Expression – Hs Myeloid v2 Panel CodeSet (NanoString Technologies; Seattle, WA, USA) was used to evaluate the expression of genes associated with myeloid innate immune system response. The following is a summary of NanoString's procedure. In brief, 100ng of each RNA sample was added to the CodeSet in hybridization buffer and incubated at 65°C for 16 hours. Purification and binding of the hybridized complexes were then carried out automatically on the nCounter Prep Station using magnetic beads derivatized with short nucleic acid sequences that are complementary to the capture and reporter probes. First, the hybridization mixture was allowed to bind to the magnetic beads via the capture probe followed by washing to remove excess reporter probes and DNA fragments that are not hybridized. The probe complexes were then

eluted off the beads and hybridized to magnetic beads complementary to the reporter probe followed by wash steps to remove excess capture probes. Finally, the purified target-probe complexes are eluted off and are immobilized in the cartridge for data collection. Data collection was carried out in the MAX System Digital Analyzer (NanoString Technologies; Seattle, WA, USA). Digital images were processed, and barcode counts tabulated in a comma-separated value (CSV) format. The raw count data was then normalized to mean of positive control probes followed by RNA content normalization to the geometric mean of housekeeping genes in the CodeSet. Data normalization was performed using nCounter Analysis Software version 4.0 (NanoString Technologies; Seattle, WA, USA). Gene set enrichment analysis (GSEA) was utilized to determine which Nanostring-defined functional pathways were regulated within the individually polarized phenotypes. Briefly, the pathway score, a weighted vector determined from t-statistics, was promoting wound reepithelialization and extracellular matrix deposition calculated for each gene against the resting M0 cells in the model [54]. Two representations of these pathway scores are presented in the data. The first, undirected global significance scores (UGS), were utilized to identify which pathways were differentially regulated in each phenotype regardless of the whether the genes were up- or down-regulated when compared to the M0 MΦs. An extension of this score, the directed global significance statistics (DGS), measures the extent to which the genes are up- or down-regulated within the given pathway. In general, a positive pathway score for a specific phenotype indicates a predominance of genes that are up-regulated within the pathway as compared to those that are down-regulated whereas a negative pathway score would indicate the reverse [54]. Additional analyses were conducted using bioDBnet Biological Database [55] and DAVID bioinformatics resources [56, 57]. The top up-regulated genes within each activated phenotype were selected and gene ontology analysis (GO). The GO processes significantly enriched ($p \leq 0.05$) were then chosen for comparison. Additional supervision of the GO process list included the elimination of GO processes related to specific disease processes, and ubiquitous immune system processes (e.g. GO:0045824: negative regulation of innate immune response) that were common to all phenotypes.

Results

Cell surface marker expression profiles provide little functional separation of the MΦs phenotypes

Six distinct MΦ functional phenotypes were produced from CD14+ monocytes, differentiated into resting M0 MΦs, and then polarized into M1 (IFN-γ/LPS), M2a (IL-4/IL-13), M2b (IC/LPS), M2c (IL-10), and M2d (IL-6/LIF) MΦ phenotypes. For simplicity of notation, these phenotypes will be referenced as M1, M2a, M2b, M2c and M2d MΦs. Following polarization, the MΦs were profiled in parallel systems-based approaches including cell surface marker analysis using flow cytometry, proteomics, transcriptomics, and metabolomics.

At 72 hours post polarization, the six MΦ phenotypes were stained with four common MΦ cell surface markers chosen based on expression profiles previously identified in the literature and focused on antigen-presenting or phagocytotic capacity of MΦ phenotypes [58] including CD40, CD86, CD163, and HLA-DR. The geometric mean of the fluorescent intensity (MFI) was corrected for background staining using unstained and fluorescence minus one (FMO) controls using a 0.1% cutoff with respect to negative controls. From the intensity of expression phenotype overlays (Fig. 1 A-D) and corrected MFI histograms (Fig. 1E-H), pro-inflammatory M1 MΦs (red bars) demonstrated elevated expression levels for CD40 (Fig 1E), CD86 (Fig. 1F), and HLA-DR (Fig. 1H), compared to resting MΦs (cyan bars). Within the alternatively activated MΦ subgroup, only the M2a MΦs (yellow bars) displayed APC functionality with the high expression levels of both CD86 (Fig. 1F) and HLA-DR (Fig. 1H). Expression of CD163 (Fig. 1G) was elevated in both M2c (gray bars) and M2d cells (purple bars) while all other phenotypes had decreased expression compared to M0 MΦs. Interestingly, M2b cell alone had decreased expression levels of HLA-DR compared to control. Taken together, M1 MΦs identified as $CD40^{high}CD86^{high}CD163^{low}HLA\text{-}DR^{high}$, M2a cells as $CD86^{high}CD163^{low}HLA\text{-}DR^{high}$, M2b MΦs as $CD163^{low}HLA\text{-}DR^{low}$, while both M2c and M2d MΦs appeared as $CD86^{low}CD163^{high}$.

Signal protein profiles demonstrate the inflammatory potential of M1 and M2b MΦs

Cytokines, chemokines, and growth factors are involved in multiple effector functions, especially the initiation and remediation of inflammation, induced during MΦ activation. To evaluate the inflammatory potential of our MΦ phenotypes, the cell culture supernatant was removed at 24 hours post-polarization and secreted protein expression measured using a multiplexed protein panel consisting of 17 cytokines, chemokines, and growth factors and depicted by the histogram bars (left y-axis) in Figure 2A-C and Figure S1A-G in the Online Supplementary Material). The box plots represent mRNA expression for each marker and associated with the right y-axis in the plots. Included within the panel are IL-10, IL-4, IL-13 and IFNγ which also served as activating factors for the M2c, M2a and M1 MΦs, respectively. As such, it was not possible to elucidate the contribution that the activating factor made to the overall concentration of the measured mediators. Therefore, an N/A was used in place of the histogram to designate specific phenotypes and factors.

As depicted in Figure 2A and Figure S1, both M1 and M2b MΦs secrete high levels of pro-inflammatory cytokines and chemokines including TNFα, IL-12p70, CCL3, CXCL10, CXCL8, and IFNα. It is noteworthy, however, that M1 MΦs generally produce more of these cytokines and chemokines than M2b cells. Additionally, both phenotypes also secrete anti-inflammatory cytokines IL-4 (Fig. S1D) and IL-13 (Fig. S1E) which are believed to mediate inflammatory responses and drive the activation of M2a MΦs [59]. The cytokines IL-1α, IL-1β and IL-6 secreted by M1 and M2b cells (Fig, 2B) while generally considered to be pro-inflammatory also demonstrate immunomodulating functions such as increasing gene expression as transcription factors [60], stimulating of T Helper (T_h) cell immune responses [61], promoting tissue repair, and regulating metabolism [62]. While these findings suggest that both M1 and M2b MΦs participate in inflammatory processes, M2b MΦs differ in that they also produce elevated levels of the anti-inflammatory mediator IL-10 (Fig. 2B). Within the broader M2 phenotypes, M2a MΦs secrete CCL2 (Fig. 2B) and GM-CSF (Fig. 2C) which are responsible for the recruitment and differentiation of immune system cells,

respectively. Interestingly, both M2a and M2b MΦs produced IFNγ (Fig. S1F) which, in addition to being a potent activator of M1 MΦs, also has been implicated in chronic inflammation, autoimmune pathologies and anti-inflammatory processes commonly associated with M2-like phenotypes [63]. Within our analysis panel, growth factors, TGF-β (Fig. 2B), PDGF-BB and VEGF-A (Fig. 2C) also exhibited differential expression within the evaluated phenotypes. Notably, all the M2 subtypes secreted TGF-β at levels above M0 and M1 MΦs, while primarily M2b MΦs and to a lesser extent M1 cells produced VEGF-A. Finally, the mean mRNA expression (represented by the dark circles in the box plots) generally reflected trends observed with the secreted protein levels. While there are some exceptions to this pattern, it is not possible to assign significance to these exceptions given the differential regulation of both RNA transcription and translation.

Global transcriptomics differentiates the MΦ functional phenotypes from the resting M0 phenotype

Hierarchical clustering (HC) was performed on the normalized expression data as an initial step to identify differences in the transcriptional profiles of the polarized MΦ phenotypes relative to the M0 parent MΦ and to visualize relative differences between the individual MΦ subtypes (Fig. S2A). Distinct separation from the M0 phenotype was observed for both the M1, M2b, M2a and M2c phenotypes although little distinction was visible between the M2d and M0 phenotypes. Within the subtypes, M1 and M2b clustered together; however, clear differences were present. M2a MΦs clustered with the M2c, M2d, and M0 phenotypes although was most closely aligned with the transcriptional profile of the M2c MΦs. As suggested by the HC analysis, MΦ polarization modulates the genetic expression of the MΦ phenotypes with the strongest effects observed for the M1, M2a and M2b MΦs. To further visualize these distinctions, the fold change for each gene was calculated relative to the M0 phenotype and the number of up- and down-regulated genes ($-1 \leq Log_2FC \geq 1$) graphed in Figure S2B. The relative number of differentially expressed genes observed for each phenotype generally mirrors the patterns identified through HC although M2d cells which exhibited far more differentially expressed genes than might be otherwise be predicted from the heatmap.

A one-way ANOVA using an adjusted p-value (FDR) cutoff of 0.05 revealed 189 significantly differentially expressed genes (SDEGs). HC analysis of these transcripts demonstrated very similar clustering patterns to those observed for the entire gene set (Fig. S3); however, constraining the HC analysis to SDEGs confirmed that the M2d phenotype has a unique transcriptome profile most similar to M2c MΦs when compared to the M0 parent cells. Principal component analysis (PCA) confirmed the HC results and demonstrated the functional separation of the individual phenotypes from the parent phenotype, as well as the close association of the M2c and M2d MΦs (Figure S4). Finally, orthogonal partial least squares discriminant analysis (OPLSDA) demonstrated clear class separation between MO MΦs and the polarized phenotypes in the cross-validated score plots (Fig. S4A-E).

Pathway Analysis and Gene Ontology (GO) Process identification Defined Biological Functionality

Gene set enrichment analysis (GSEA) was utilized to determine which Nanostring-defined functional pathways were regulated within the individually polarized phenotypes. Analysis of the undirected global significance scores (UGS) revealed that all the measured pathways were differentially regulated in comparison to the resting M0 parent cells for each individual phenotype (solid colored plots in the radar graphs in Figs 3A- E). Similar to the pattern observed for HC results, the relative magnitude of pathway regulation in M1 cells (Fig. 3A) was similar to the M2b MΦs (Fig. 3C) A similar trend was seen for the M2a, M2c and M2d MΦs (Fig. 3B, D & E), although the observed UGS magnitude was approximately half that observed for the M1 and M2b cells. Despite the phenotypic differences in pathway regulation, these results confirm the efficacy of the selected polarizing stimuli to initiate transcriptional programs significantly different than the M0 MΦs.

An extension of the UGS score, the directed global significance statistics (DGS), measured the extent to which the pathway genes were up- or down-regulated within the given pathway thus indicating the importance of the pathways in the functional profile of each phenotype (white hashed plots in the radar graphs in Figure 3). Positive DGS values (hashed pattern extending beyond the thick maroon circle)

therefore denote biologically relevant pathways for each individual phenotype whereas negative DGS (hashed pattern inside the thick maroon circle) suggests a down-regulation of that pathway. Combining these measures with the GO process analysis (Figures 3A-E) provided unique insight into the biological functionality of the polarized phenotypes defined by the transcriptional profiles.

Of the 19 functionally defined pathways, the angiogenesis, complement activation, differentiation of myeloid cells, and T_h2 response pathways appear to be downregulated in the M1 cells (Fig. 3A). GSEA identified 97 SDEGs ($(-1 \leq Log_2FC \geq 1$ and $p \leq 0.05)$ consisting of which 41% and 12 % IFN-γ responsive and LPS-responsive genes, respectively. Within the IFN-γ responsive genes, interferon pathway genes, IRF1, IRF7, IRF8 and ISG15, are known transcriptional enhancers of genes associated with antigen presentation and T_h1 responses (e.g. CD40 and CD86), cytokine and chemokine signaling (e.g. TNF, CXCL9, CCL4, CCL8 and STAT1), and pathogen response (e.g. IL18 and IRG1) [15, 64]. These finding are generally mirrored in the GO processes (Fig. 4A); however, additional processes, such as the regulation of NO processes and the HIF-1α signaling pathway, highlight the role of metabolic immunomodulation within M1 MΦs. These SDEGs and associated upregulated pathways are consistent with defined pro-inflammatory and antimicrobial effector functions associated with M1 polarization.

While IFN-γ and LPS are considered potent MΦ activators, the IL-4 and IL-14 stimuli utilized for M2a polarization are considered mild activators [65]. Consequently, M2a MΦs exhibited a remarkably different pathway profile than the M1 MΦs. While all 19 pathways were differentially regulated when compared to M0 cell, only the T-cell activation, T_h2 activation, metabolism, and ECM remodeling pathways were upregulated (Fig. 3B). This trend was also reflected in the GSEA results in that of the 83 SDEG identified only 36% of these transcripts were upregulated with 84% being downregulated. Despite being upregulated when compared to M0 MΦs, the T-cell and T_h2 activation pathways did not exhibit any SDEGs using our inclusion criteria. The ECM remodeling pathway contained known metalloproteinase genes, ADAM19 and MMP12, whereas the metabolism pathway contained the common M2a-associated transcripts of TGM2,

FABP4, and PTGS1. Additionally, the identified GO processes (Fig. 4B) heavily favored the tissue-reparative, pro-fibrotic, pro-angiogenic, and phagocytic functions [1, 25-27]. Additionally, the most upregulated genes, CCL17, CCl22 and CCL18, support the generally accepted role that M2a MΦs play in cellular proliferation, ECM remodeling, and tissue repair [66, 67].

Many similarities in the DGS patterns were observed between the M1 and M2b phenotypes; however, the M2b cells downregulated antigen presentation, cell migration and adhesion, complement activation, and T_h2 response pathways (Fig. 3C). Chemokine signaling, the most upregulated pathway, was associated with prominent SDEGs identified in the enrichment analysis and supportive of many other functional pathways. For example, chemokines CXCL2, CXCL3, and CXCL5 promote angiogenesis through the recruitment of angiogenic neutrophils while CCL5, CCL8, and CXCL9 transcripts support the recruitment and differentiation of myeloid cells necessary for tissue remodeling functions. Of these chemokines, CXCL2, CXCL3, and CXCL5 are only differentially regulated within the M2b MΦs suggesting a potential role for FcγR ligation in the promotion of angiogenesis in this phenotype [16]. Due to the shared LPS stimulus, M1 and M2b cells exhibited many overlapping GO processes (Fig. 4A & C), especially those that are relevant to antimicrobial responses [68], and inflammatory processes. Despite these similarities, other highly enriched GO processes for M2b MΦs (Fig. 4C) highlighted key differences in these phenotypes. The GO processes of leukocyte adhesion to vascular endothelial cells, regulation of leukocyte migration, positive regulation of neutrophil extravasation, and connective tissue replacement in inflammatory wound healing support cellular functionality associated with angiogenesis, myeloid cell regulation and tissue remodeling identified for M2b polarized MΦs.

The pathway regulation pathways observed for M2c MΦs also implied, like M2a MΦs, that IL-10 is a mild activating stimulus. Of the 19 measured pathways, nine had DGS scores demonstrating upregulation of the pathways compared to the M0 parent cells. Interestingly, many of the identified SDEGs for this phenotype support much broader effector functions such as the resolution of inflammation (DUSP1, SOCS3, S100A8,

S100A9, and TNFRSF1A), the regulation of vascular insult and neutrophil chemotaxis (S100A8 and S100A9), and the protection against apoptosis and oxidative stress (IER3 and TNFRSF1B) [26]. Additionally, CD163 and MerTk resolve inflammation as scavengers for oxidative hemoglobin (Hb) and apoptotic cells, respectively [69, 70]. Identified Go processes suggest biological functionality consistent with the promotion of angiogenesis (e.g. Tie signaling pathway), phagocytosis and efferocytosis, and numerous processes supportive of ECM remodeling.

At first glance, it appeared that M2d MΦs regulated pathways in a similar way to M2c cells apart from TLR signaling and ECM remodeling. Moreover, their transcriptional profile suggested overlapping effector functions such as the resolution of inflammation (DUSP1, SOCS3, THBD, and CD163) and immune suppression (CCL8). In contrast, M2d MΦs differentially regulated many known pro-angiogenic markers such as ENPP2, SPHK1, CXCL2, and CXCL3. Furthermore, 9 of the top 17 GO processes directly relate to angiogenic processes. Of the remaining 8 listed processes, 6 contribute to ECM remodeling. Overall, these results are consistent with current research linking M2d MΦs to effector functions observed for TAMs [12, 27, 39, 71].

Untargeted Metabolomics of Five Polarized MΦ Phenotypes Identifies Biomarkers of Shared and Unique Profiles Relative to the Parent, Resting MΦ Phenotype.

Global metabolomics profiles of the parent, resting MΦ phenotype (M0) and five polarized MΦ phenotypes identified 498 compounds of known identity, normalized to cell count. The top 50 metabolites as determined by ANOVA analysis ($p < 0.05$) depicted in the dendrogram (Figure S5) provided statistical separation between the individual phenotypes. Metabolites that differentiated the M1 MΦs from the M2 polarized subtypes consisted primarily of lipids and metabolites associated with alanine, tyrosine and phenylalanine metabolism; however, M1 and M2b cells clustered together on metabolites related to tryptophan and nicotinamide metabolism. While M2a, M2c and M2d demonstrated similar clustering, metabolite differences suggested differential flux through amino acid pathways. MΦ metabotype clustering was also determined

through OPLS-DA and represented in the cross-validated score plots (inset plots in Figure 5A.1, B.1, C.1, D.1, and E.1). Separation along the x-axis (T score or between phenotype variation) in the cross-validated score plots supported metabotype cluster separation between each polarized MΦ and the M0 parent cells, while y-axis scores (orthogonal T score or within phenotype variation) reflected the variation observed within the individual samples of a specific phenotype. Generally, separation between classes along the x-axis suggests that the measured metabolites are predictive of MΦ metabotype. This distinction, however, is dependent upon minimal mathematical separation between the T scores and orthogonal T scores. The larger mathematical differences between these values observed in this data warrants additional analysis and may indicate uncertainty in the metabotype prediction on the basis of cross-validation scores alone [53].

The S-plots shown in Figures 5A.1-E.1 compare model contributions from the magnitude of the metabolite measurements (covariance; x-axis) to the reliability of the measurements (correlation; y-axis). Larger covariance scores, $-0.2 \leq \text{covariance} \geq 0.2$, differentiate metabolites that have peak intensity values significantly different from those that exhibit low dynamic ranges. Larger correlation scores ($-0.6 \leq \text{covariance} \geq 0.6$) indicate statistical reliability while the positive and negative designations of the correlation values can provide some indication as to comparative metabolic flux of specific metabolites through metabolic pathways. Therefore, biochemically significant metabolites with predictive value can be extracted from S-plots by selecting points that meet these criteria [53]. Using these guidelines, three metabolites of interest were selected for each phenotype (Figure 5A.2-E.2).

Consistent with previous research, selected metabolites (Fig. 5A.2) from the M1 MΦs S-plot (Fig. 5A.1) confirmed metabolic investment in anti-microbial function with itaconate accumulation (0.91) and anti-oxidant capacity evidenced by tryptophan consumption (-0.97) and kynurenine accumulation (0.93) [72]. The prevalence of metabolites with lower correlation scores ($-0.6 < p(corr) < 0.6$) in M2a MΦ S-plot (Fig. 5B.1) suggests some degree of metabolic similarity to the resting M0 cells. Of the selected metabolites (Fig. 5B.2), both cysteine-GSSG (0.42) and myo-inositol (0.42) and UDP-GlcNAc metabolites, suggest a role for

glutathione recycling and N-glycosylation, respectively, in M2a functionality [42, 73]. Like M1 cells, the M2b MΦs S-plot (Fig. 5C.1) exhibited strong antioxidant metabotype correlation demonstrated with the accumulation of quinolinate (0.81) and kynurenine (0.82) (Fig. 5C.2), while the decreased correlation score of acetylcarnitine (-0.83) suggested differential regulation of OXPHOS in M2b cells relative to M0 MΦs. M2c and M2d MΦs, also demonstrated metabolic similarity to the parent M0 cells (Fig. 5D.1 and 5E.1). Of the depicted metabolites, glutamate correlation values in both M2c (-0.58) and M2d cells (-0.55) suggest that glutamate is consumed at higher compared to M0 cells.

In order to completely elucidate the role of cellular metabolism in MΦ functionality, it is important to also consider metabolic differences and similarities between the individual phenotypes. Shared and unique structure (SUS) graphs were employed to provide a concise way to visualize the OPLSDA outcomes between the M1 MΦ and each of the M2 MΦ subtypes (Fig. 6A.1, B.1, C.1, and D.1). For example, by plotting the correlation from the predictive component from the M0 versus M1 model and the M0 versus M2a model, metabolic biomarkers can be identified that are not only uniquely correlated to the M1 and M2a MΦs but also have shared differentiation from the parent MO phenotype. Associated unique and shared biomarkers and correlation scores are shown in matching tables (Fig. 6A.2, B.2, C.2, and D.2). Additionally, direct comparisons were made between the M1 MΦ and each of the M2 MΦ subtypes and the statistically significant metabolites (FC>2.0 and $p<0.05$) are depicted in the volcano plots (Fig. 6A.3, B.3, C.3, and D.3).

Two distinct metabolic patterns were apparent from the SUS plot analysis and the statistically significant metabolites in the volcano plot comparisons. First, M1 MΦs differentially regulate amino acid pathways when compared to the M2 subtypes. The role of tryptophan metabolism in M1 MΦs compared to M2a, M2c and M2d subtypes was clearly demonstrated by the accumulation of kynurenine (0.93), 3-formylindole (0.92), N-formylanthranillic acid, and quinolinate (0.85) metabolites, and the diminished pool of tryptophan (-0.97) (. Fig. 6A.1-3, C.1-3, D.1-3). Tryptophan metabolism was found to be significant for both M1 and M2b phenotypes as tryptophan pathway metabolites identified as shared between the two phenotypes in the

SUS analysis (Fig. 6B.1, 2). The diminished pools of 4-guanidinobutanoate in all the M2 subtypes along with accumulation in M1 cells (0.83) implied that arginine metabolism was also differentially regulated between M1 MΦs and the M2 activated MΦs and additionally supported by decreased amounts of other arginine pathway metabolites including N'1-acetylspermidine in M2a (-0.87) and M2d cells (-0.76) and the accumulation of creatine phosphate in M1 MΦs (0.75) [74]. Metabolites unique to M1 in comparison to M2b cells, N-acetylglutamine (0.70) (SUS analysis; Fig. 6 B.1, 2) and acetylcarntine (volcano plot; Fig. B.3), highlight potential differences in glutamate and branch-chain amino acid metabolism [75].

Differences in pyrimidine and lipid metabolism evidenced by negative correlation of uracil (M2a (-0.61); M2b (-0.66) and M2c (-0.72)), and cytosine (M2c (-0.76) and M2d (-0.63)) metabolites suggested differential regulation of pyrimidine metabolism between M1 MΦs and alternatively activated phenotypes [42, 76, 77]. Although it should be noted that these differences are not uniform in all the M2 subtypes implying that flux through pyrimidine metabolism is complex. Another defining feature of M1 polarization is the accumulation of citrate due to a broken TCA cycle which leads to fatty acid and itaconate synthesis [42]. The accumulation of fatty acids and their derivatives in M1 MΦs and corresponding negative correlations within the M2 phenotypes (e.g. palmitoyl-myristoyl-glycerol (M2a = -0.72), N-stearoyl-sphingosine (M2a = -0.81 and M2b = -0.70), 1-stearoyl-2-oleoyl-GPS (M2c = -0.64 and M2d = -0.68), and 1-stearoyl-2-linoleoyl-GPS (M2d = -0.63) (Fig. 6B.3 and 6D.2,3; Fig. S6 and S7) was consistent with observed phenotypic differences in lipid metabolism. Additionally, itaconate also proved to be an effective biomarker to differentiate between the M1 and M2a MΦs (Fig. 6 A.1-3) [42, 77] while a similar accumulation pattern with itaconate observed with M1 (0.91) and M2b (0.91) cells highlights a potential shared anti-microbial function (Fig. 6B.1, 2).

Metabolic Pathway Analysis Defined Unique Metabotypes for Each Individual Polarized Phenotype

To more comprehensively elucidate the metabotype of the polarized MΦs, Metaboanalyst software was used to identify specific metabolic pathways that are active within the individual phenotypes. The MΦ

metabolomes for each phenotype (Figure 7) are illustrated in topological maps organized by p-value from the pathway enrichment analysis (y-axis) versus the impact scores from the pathway topology analysis (x-axis) while the node color and size are indicative of p-value significance and pathway impact, respectively. Additionally Figure 8 contains genes transcripts that are associated with specific metabolic pathways with upregulated genes and downregulated SDEGs relative to the M0 parent cells are colored in green and blue, respectively. Finally, a comprehensive summary of this metabolic analysis is illustrated in Figure 9. Each of the colored boxes above the listed metabolite represents the fold change of that metabolite in the M1, M2a, M2b, M2c and M2d phenotypes, illustrated from left to right in set of boxes, relative to M0 MΦs. Numerical values corresponding to the color scale is included in Tables S1 and S2.

One defining feature of polarized MΦs is the utilization of glucose and aerobic glycolysis to support ATP production [10, 42, 44]. The gene transcript, FBP1, that mediates the interconversion between fructose 6-phosphate and fructose 1,6-bisphosphate was significantly down regulated in all of the polarized MΦs (Fig. 8A) confirms this assertion [78] ; however studies have shown that M1 MΦs consume more glucose than M2a or M2c cells [44] suggesting phenotypic variation in the importance of glycolysis in MΦ immunometabolism and may in part explain the accumulation of glucose observed in the M2c and M2d MΦs (Fig. 9). Additionally, M1 and M2b cells downregulated the FBP1 transcript considerably more than the other phenotypes. Furthermore, the upregulation of CD44 in both of these phenotypes (Fig. 8A), a prominent cancer cell marker, has been shown to enhance glycolysis and flux into the PPP [79, 80] and could play a similar role in M1 and M2b MΦ metabolism and the overall importance of the pathway. Another prominent feature of M1 cells is the diversion of glycolytic intermediates into the PPP to fuel the production nucleotides, through pyrimidine and purine pathways, secondary metabolic intermediates and the nucleotide substrate NADPH [17, 42]. The accumulation of glycerate (Fig. 9: PPP) in the M1, M2b and M2d MΦs is suggestive of flux into the PPP for each of these phenotypes. From the topography analysis, the most statistically significantly pathway observed was pyrimidine metabolism for both M1 and M2b MΦs (Fig. 7A and C; Fig. 9) while the purine pathway was most prevalent for M2d (Fig. 7E; Fig. 9). It is probable that the

function of these pathways is similar for both the M1 and M2b phenotypes given their shared inflammatory signatures; however recent research contends that TAMs (M2d cells) utilize pyrimidine and purine nucleotides to promote chemotherapeutic resistance and tumor cell growth, respectively [11, 81]. Another prominent function of the PPP is the generation of ROS and the maintenance of a balanced cellular redox state, While ROS levels were not directly evaluated in this study, the upregulation of thioredoxin (TXN) in M1 cells (Fig. 8D) which is activated with a redox microenvironment lends support for metabolic flux through the PPP within M1 MΦs [82].

Arguably the most notable metaboype feature of M1 polarization is the decoupled TCA after citrate and succinate. The accumulation of itaconate from excess citrate (Fig. 9: TCA) mediated through the upregulation of IRG1 (Fig. 8A) was observed in this data. The accumulation of itaconate (Fig. 9: TCA) inhibits succinate dehydrogenase resulting in succinate accumulation (Fig 9: TCA) needed for HIF-1a stabilization [41]. The TCA cycle metabolism also demonstrated statistical significance in the pathway analysis (Fig. 7C). From the gene set analysis, M2b cells exhibited IRG1 upregulation (Fig. 8A) along with itaconate accumulation (Fig. 9: TCA). While these findings might suggest that M2b MΦs have a decoupled TCA like the M1 phenotype, M2b cells did not accumulate succinate (Fig. 9: TCA). Although the accumulation of itaconate is generally regarded as the SDH inhibitor necessary for the TCA break at succinate, these finding suggests this relationship may be more complex. The remaining M2 subtypes, M2a, M2c and M2D all demonstrated metabolic flux patterns consistent with an intact TCA.

Other highly impacted pathways included sphingolipid (Fig. S6B and C) and glycerophospholipid metabolism (Fig. S7A and B). One important need for glycerophospholipids (Fig. S7A and B) in inflammatory M1 MΦs is the production of prostaglandins and thromboxane which is mediated through PTGS2 (Fig. 8D) in the arachidonic acid metabolic pathway [83]. Additionally, the gene transcripts ALOX5 and LTA4H (Fig. 8D) that regulate the production of specialized pro-resolving mediators (SPMs) such as lipoxins [84] are down regulated and have been shown to promote MΦ inflammation in Nlrp3

inflammasome-dependent manner [85] and inhibit FAO and the mitochondrial electron transport chain [86, 87]. Additionally, arachidonic acid metabolism was impacted in M2a with the upregulation of PTGS1 and ALOX15 (Fig.8D). PTGS1, like PtGS2, also mediates both prostaglandins and thromboxane synthesis; however, PTGS1 is constitutively expressed whereas PTGS2 is an early immune system response to acute injury [88]. ALOX15 facilities the conversion of arachidonic acid to 15-hydroxyeicosatetraenoic acid (15(S)-HETE)) and 12(S)-HETE which activate PPARG an essential marker of M2a polarization involved in the activation of CD206 and CD36 [89]. Sphingolipid metabolism was also highly impacted with the M2-like subtypes (Fig. 7B-E); however, these phenotypes presented with significantly diminished pools of sphingomyelins and ceramides (Figure S6B and C). Ceramide consumption through lysosomal lipolysis in M2a cells has been shown to remove OXPHOS inhibition [77, 86, 87]. Additionally, the consumption of fatty acids and glycerophospholipids for all M2 subtypes (Fig. S6A and Fig. S7A and B), the significantly diminished metabolic pools of fatty acid carnitines especially in M2b MΦs (Fig. S8), and the upregulation of FABP4 (M2a), LPL (M2a) and CD36 (M2c and M2d) (Fig. 8C) are indicative of active FAO.

Amino acid metabolism was demonstrated to be highly significant for each of the polarized phenotypes. The β-alanine metabolic pathway was highly impacted pathway for the M1, M2a, M2b and M2d MΦs was (Fig. 7A, B, C and E). Proposed sources of β-alanine include arginine metabolism via polyamine metabolism in M2a cells [42] or the degradation of 5,6-dihydrouridine in the pyrimidine pathway (Fig. 9) for M1, M2b and M2d MΦs. [90] . Two additional amino acid pathways were found to have shared significance ($p < 0.05$) among the MΦ phenotypes, specifically, arginine and proline metabolism and alanine, aspartate and glutamate metabolism (Fig. 7A-E). Glutamine metabolism is known to play a significant role in the replenishment of TCA metabolites depleted as a result of an uncoupled TCA in M1 MΦs. Isotope labeling experiments have confirmed that glutamate contribute to α-ketoglutarate and to fumarate through the arginosuccinate shunt [42, 91]. Additionally, the metabolic flux of glutamine into arginine metabolism is essential to NO production through citrulline for M1 and potentially M2b cells (Fig. 9: Urea Cycle) [25, 42, 91]. Furthermore, both glutamate and aspartate are needed for the *de nova* synthesis of purines and

pyrimidines and likely significant for M1, M2b and M2d cells (Fig, 9) [90]. Aspartate facilitates turnover with the decoupled TCA through alanine to produce pyruvate and through the arginosuccinate shunt by replenish fumarate (Fig. 9: TCA). As previously mentioned, M2a MΦs demonstrate active glycolysis which is used to supply the TCA cycle; however, M2a polarization has been shown to be unaffected during glucose deprivation suggesting that other metabolic pathways, such as glutaminolysis, can be utilized to support the TCA and oxidative metabolism [92]. In addition to TCA support, glutamine consumption (Fig. 7B, Fig. 9) combined with the diversion of glycolytic intermediates into the hexosamine biosynthesis pathway supports N-glycosylation as evidenced by the accumulation of UDP-glucose, UDP-galactose and UDP-glucuronate (Fig. 9: Amino Sugar Metabolism) in M2a cells [42]. Another role for arginine and proline metabolism is as a part of the urea cycle to support collagen synthesis via proline. Given that both proline and hydroxyproline demonstrate a similar metabolite flux pattern in all the M2 subtypes (Fig. 9: Urea Cycle), it is probable these phenotypes participate in collagen synthesis [93]. Finally, both arginine and glycine can be diverted to synthesis creatine through guanidinoacetate which had been shown to suppress IFN-γ responses while facilitating IL-4 polarization in MΦs [74].

The upregulation of CD38, IDO1 and NAMPT (Fig. 8A and B) and potential aspartate flux through quinolinate reaffirmed previously identified results highlighting the importance of tryptophan and nicotinamide metabolism within the M1 and M2b MΦs (Fig. 9). Additionally, the accumulation of kynurenate in M2d cells (Fig. 9: Tryptophan Metabolism) suggested a role for this pathway in this phenotype as well. Glycine, serine and threonine metabolism (Fig. 7A and Fig 9) was only identified as significant within the M1 MΦs and not surprising given that glycine and serine have been identified among the most highly produced and consumed amino acids, respectively, in LPS-stimulated MΦs [94].

In the M2b and M2c phenotypes, both taurine, cysteine and methionine amino acid pathways presented as impacted pathways (Fig. 7C and D). Within the metabolism data, both taurine and hypotaurine were significantly decreased compared to the M0 parent cells (Fig. 9: Methionine, Cysteine, & Taurine). In

addition to feeding taurine, cysteine directly feeds glutathione metabolism an essential pathway for ROS mediation (Fig. 9: Glutathione Metabolism). Moreover, both phenotypes exhibited diminished levels of oxidized glutathione and γ-glutamylamino acids which are produced as a part of the γ-glutamyl cycle (Fig. 9).

References

1. Stein, M., Keshav, S., Harris, N., Gordon, S. (1992) Interleukin 4 potently enhances murine macrophage mannose receptor activity: a marker of alternative immunologic macrophage activation. Journal of Experimental Medicine 176, 287-292.
2. Goerdt, S., Politz, O., Schledzewski, K., Birk, R., Gratchev, A., Guillot, P., Hakiy, N., Klemke, C. D., Dippel, E., Kodelja, V., Orfanos, C. E. (1999) Alternative versus Classical Activation of Macrophages. Pathobiology 67, 222-226.
3. Stout, R. D., Jiang, C., Matta, B., Tietzel, I., Watkins, S. K., Suttles, J. (2005) Macrophages sequentially change their functional phenotype in response to changes in microenvironmental influences. The Journal of Immunology 175, 342-349.
4. Gosselin, D., Link, V. M., Romanoski, C. E., Fonseca, G. J., Eichenfield, D. Z., Spann, N. J., Stender, J. D., Chun, H. B., Garner, H., Geissmann, F. (2014) Environment drives selection and function of enhancers controlling tissue-specific macrophage identities. Cell 159, 1327-1340.
5. Lavin, Y., Winter, D., Blecher-Gonen, R., David, E., Keren-Shaul, H., Merad, M., Jung, S., Amit, I. (2014) Tissue-resident macrophage enhancer landscapes are shaped by the local microenvironment. Cell 159, 1312-1326.
6. Martinez, F. O., Sica, A., Mantovani, A., Locati, M. (2008) Macrophage activation and polarization. Front Biosci 13, 453-461.
7. Mantovani, A., Sica, A., Sozzani, S., Allavena, P., Vecchi, A., Locati, M. (2004) The chemokine system in diverse forms of macrophage activation and polarization. Trends in Immunology 25, 677-686.
8. Mosser, D. M. and Edwards, J. P. (2008) Exploring the full spectrum of macrophage activation. Nat Rev Immunol 8, 958-969.
9. Koh, T. J. and DiPietro, L. A. (2011) Inflammation and wound healing: the role of the macrophage. Expert Reviews in Molecular Medicine 13.
10. Penny, H. L., Sieow, J. L., Adriani, G., Yeap, W. H., See Chi Ee, P., San Luis, B., Lee, B., Lee, T., Mak, S. Y., Ho, Y. S. (2016) Warburg metabolism in tumor-conditioned macrophages promotes metastasis in human pancreatic ductal adenocarcinoma. Oncoimmunology 5, e1191731.
11. Halbrook, C. J., Pontious, C., Kovalenko, I., Lapienyte, L., Dreyer, S., Lee, H.-J., Thurston, G., Zhang, Y., Lazarus, J., Sajjakulnukit, P. (2019) Macrophage-released pyrimidines inhibit gemcitabine therapy in pancreatic cancer. Cell metabolism 29, 1390-1399. e6.
12. Cao, W., Peters, J. H., Nieman, D., Sharma, M., Watson, T., Yu, J. (2015) Macrophage subtype predicts lymph node metastasis in oesophageal adenocarcinoma and promotes cancer cell invasion in vitro. British journal of cancer 113, 738-746.
13. Gibbings, S. L., Goyal, R., Desch, A. N., Leach, S. M., Prabagar, M., Atif, S. M., Bratton, D. L., Janssen, W., Jakubzick, C. V. (2015) Transcriptome analysis highlights the conserved difference between embryonic and postnatal-derived alveolar macrophages. Blood 126, 1357-1366.
14. Vogelpoel, L. T. C., Hansen, I. S., Rispens, T., Muller, F. J. M., van Capel, T. M. M., Turina, M. C., Vos, J. B., Baeten, D. L. P., Kapsenberg, M. L., de Jong, E. C., den Dunnen, J. (2014) Fc gamma receptor-TLR cross-talk elicits pro-inflammatory cytokine production by human M2 macrophages. Nature communications 5, 5444-5444.

15. Fan, J.-B., Miyauchi-Ishida, S., Arimoto, K.-i., Liu, D., Yan, M., Liu, C.-W., Győrffy, B., Zhang, D.-E. (2015) Type I IFN induces protein ISGylation to enhance cytokine expression and augments colonic inflammation. Proceedings of the National Academy of Sciences 112, 14313-14318.
16. Elshabrawy, H. A., Chen, Z., Volin, M. V., Ravella, S., Virupannavar, S., Shahrara, S. (2015) The pathogenic role of angiogenesis in rheumatoid arthritis. Angiogenesis 18, 433-448.
17. O'Neill, L. A. J., Kishton, R. J., Rathmell, J. (2016) A guide to immunometabolism for immunologists. Nat Rev Immunol 16, 553-565.
18. Lachmandas, E., Boutens, L., Ratter, J. M., Hijmans, A., Hooiveld, G. J., Joosten, L. A., Rodenburg, R. J., Fransen, J. A., Houtkooper, R. H., Van Crevel, R. (2017) Microbial stimulation of different Toll-like receptor signalling pathways induces diverse metabolic programmes in human monocytes. Nature microbiology 2, 16246.
19. Murray, P. J., Allen, J. E., Biswas, S. K., Fisher, E. A., Gilroy, D. W., Goerdt, S., Gordon, S., Hamilton, J. A., Ivashkiv, L. B., Lawrence, T., Locati, M., Mantovani, A., Martinez, F. O., Mege, J. L., Mosser, D. M., Natoli, G., Saeij, J. P., Schultze, J. L., Shirey, K. A., Sica, A., Suttles, J., Udalova, I., van Ginderachter, J. A., Vogel, S. N., Wynn, T. A. (2014) Macrophage Activation and Polarization: Nomenclature and Experimental Guidelines. Immunity 41, 14-20.
20. Porta, C., Riboldi, E., Ippolito, A., Sica, A. (2015) Molecular and epigenetic basis of macrophage polarized activation. Seminars in Immunology 27, 237-248.
21. Krausgruber, T., Blazek, K., Smallie, T., Alzabin, S., Lockstone, H., Sahgal, N., Hussell, T., Feldmann, M., Udalova, I. A. (2011) IRF5 promotes inflammatory macrophage polarization and T H 1-T H 17 responses. Nature immunology 12, 231.
22. Wilgus, T. A. (2018) Alerting the body to tissue injury: The role of alarmins and DAMPs in cutaneous wound healing. Curr Pathobiol Rep 6, 55-60.
23. Murray, P. J. and Wynn, T. A. (2011) Protective and pathogenic functions of macrophage subsets. Nature Reviews Immunology 11, 723-737.
24. Rak, G. D., Osborne, L. C., Siracusa, M. C., Kim, B. S., Wang, K., Bayat, A., Artis, D., Volk, S. W. (2016) IL-33-Dependent Group 2 Innate Lymphoid Cells Promote Cutaneous Wound Healing. Journal of Investigative Dermatology 136, 487-496.
25. Edwards, J. P., Zhang, X., Frauwirth, K. A., Mosser, D. M. (2006) Biochemical and functional characterization of three activated macrophage populations. Journal of Leukocyte Biology 80, 1298-1307.
26. Lurier, E. B., Dalton, D., Dampier, W., Raman, P., Nassiri, S., Ferraro, N. M., Rajagopalan, R., Sarmady, M., Spiller, K. L. (2017) Transcriptome analysis of IL-10-stimulated (M2c) macrophages by next-generation sequencing. Immunobiology 222, 847-856.
27. Duluc, D., Delneste, Y., Tan, F., Moles, M.-P., Grimaud, L., Lenoir, J., Preisser, L., Anegon, I., Catala, L., Ifrah, N., Descamps, P., Gamelin, E., Gascan, H., Hebbar, M., Jeannin, P. (2007) Tumor-associated leukemia inhibitory factor and IL-6 skew monocyte differentiation into tumor-associated macrophage-like cells. Blood 110, 4319-4330.
28. Gordon, S. (2003) Alternative activation of macrophages. Nature Reviews Immunology 3, 23-35.
29. Liu, Y.-C., Zou, X.-B., Chai, Y.-F., Yao, Y.-M. (2014) Macrophage polarization in inflammatory diseases. Int J Biol Sci 10, 520-529.
30. Jetten, N., Verbruggen, S., Gijbels, M. J., Post, M. J., De Winther, M. P. J., Donners, M. M. P. C. (2014) Anti-inflammatory M2, but not pro-inflammatory M1 macrophages promote angiogenesis in vivo. Angiogenesis 17, 109-118.
31. Todd, R., Donoff, B. R., Chiang, T., Chou, M. Y., Elovic, A., Gallagher, G. T., Wong, D. T. (1991) The eosinophil as a cellular source of transforming growth factor alpha in healing cutaneous wounds. The American journal of pathology 138, 1307-1313.
32. Sutterwala, F. S., Noel, G. J., Salgame, P., Mosser, D. M. (1998) Reversal of Proinflammatory Responses by Ligating the Macrophage Fcγ Receptor Type I. The Journal of Experimental Medicine 188, 217.
33. Gerber, J. S. and Mosser, D. M. (2001) Reversing lipopolysaccharide toxicity by ligating the macrophage Fcγ receptors. The Journal of Immunology 166, 6861-6868.
34. Anderson, C. F. and Mosser, D. M. (2002) A novel phenotype for an activated macrophage: the type 2 activated macrophage. Journal of leukocyte biology 72, 101-106.

35. Nishiguchi, T., Ito, I., Lee, J. O., Suzuki, S., Suzuki, F., Kobayashi, M. (2017) Macrophage polarization and MRSA infection in burned mice. Immunology and cell biology 95, 198-206.
36. Sahin, K. B., Hesketh, M., West, Z. E., Murray, R. Z. (2017) Altered macrophage phenotypes impair wound healing. Wound Practice and Research 25, 166-171.
37. Ohlsson, S. M., Linge, C. P., Gullstrand, B., Lood, C., Johansson, Å., Ohlsson, S., Lundqvist, A., Bengtsson, A. A., Carlsson, F., Hellmark, T. (2014) Serum from patients with systemic vasculitis induces alternatively activated macrophage M2c polarization. Clinical Immunology 152, 10-19.
38. Gabriel, V. A., McClellan, E. A., Scheuermann, R. H. (2014) Response of human skin to esthetic scarification. Burns 40, 1338-1344.
39. Galdiero, M. R., Garlanda, C., Jaillon, S., Marone, G., Mantovani, A. (2013) Tumor associated macrophages and neutrophils in tumor progression. Journal of cellular physiology 228, 1404-1412.
40. Artyomov, M. N., Sergushichev, A., Schilling, J. D. (2016) Integrating immunometabolism and macrophage diversity. Seminars in immunology 28, 417-424.
41. Tannahill, G. M., Curtis, A. M., Adamik, J., Palsson-McDermott, E. M., McGettrick, A. F., Goel, G., Frezza, C., Bernard, N. J., Kelly, B., Foley, N. H., Zheng, L., Gardet, A., Tong, Z., Jany, S. S., Corr, S. C., Haneklaus, M., Caffrey, B. E., Pierce, K., Walmsley, S., Beasley, F. C., Cummins, E., Nizet, V., Whyte, M., Taylor, C. T., Lin, H., Masters, S. L., Gottlieb, E., Kelly, V. P., Clish, C., Auron, P. E., Xavier, R. J., O'Neill, L. A. J. (2013) Succinate is an inflammatory signal that induces IL-1β through HIF-1α. Nature 496, 238-242.
42. Jha, Abhishek K., Huang, Stanley C.-C., Sergushichev, A., Lampropoulou, V., Ivanova, Y., Loginicheva, E., Chmielewski, K., Stewart, Kelly M., Ashall, J., Everts, B., Pearce, Edward J., Driggers, Edward M., Artyomov, Maxim N. (2015) Network Integration of Parallel Metabolic and Transcriptional Data Reveals Metabolic Modules that Regulate Macrophage Polarization. Immunity 42, 419-430.
43. Michelucci, A., Cordes, T., Ghelfi, J., Pailot, A., Reiling, N., Goldmann, O., Binz, T., Wegner, A., Tallam, A., Rausell, A. (2013) Immune-responsive gene 1 protein links metabolism to immunity by catalyzing itaconic acid production. Proceedings of the National Academy of Sciences 110, 7820-7825.
44. Rodríguez-Prados, J.-C., Través, P. G., Cuenca, J., Rico, D., Aragonés, J., Martín-Sanz, P., Cascante, M., Boscá, L. (2010) Substrate Fate in Activated Macrophages: A Comparison between Innate, Classic, and Alternative Activation. The Journal of Immunology 185, 605.
45. Palsson-McDermott, E. M., Curtis, A. M., Goel, G., Lauterbach, M. A. R., Sheedy, F. J., Gleeson, L. E., van den Bosch, M. W. M., Quinn, S. R., Domingo-Fernandez, R., Johnston, D. G. W., Jiang, J.-K., Israelsen, W. J., Keane, J., Thomas, C., Clish, C., Vander Heiden, M., Xavier, R. J., O'Neill, L. A. J. (2015) Pyruvate kinase M2 regulates Hif-1α activity and IL-1β induction and is a critical determinant of the warburg effect in LPS-activated macrophages. Cell metabolism 21, 65-80.
46. Freigang, S. (2016) The regulation of inflammation by oxidized phospholipids. European journal of immunology 46, 1818-1825.
47. Malandrino, M. I., Fucho, R., Weber, M., Calderon-Dominguez, M., Mir, J. F., Valcarcel, L., Escoté, X., Gómez-Serrano, M., Peral, B., Salvadó, L. (2015) Enhanced fatty acid oxidation in adipocytes and macrophages reduces lipid-induced triglyceride accumulation and inflammation. American Journal of Physiology-Endocrinology and Metabolism 308, E756-E769.
48. Rath, M., Müller, I., Kropf, P., Closs, E. I., Munder, M. (2014) Metabolism via arginase or nitric oxide synthase: two competing arginine pathways in macrophages. Frontiers in immunology 5, 532.
49. Xue, C., Liu, Y., Wang, J., Zhang, R., Zhang, Y., Zhang, J., Zhang, Y., Zheng, Z., Yu, X., Jing, H., Nosaka, N., Arai, C., Kasai, M., Aoyama, T., Wu, J. (2009) Consumption of medium- and long-chain triacylglycerols decreases body fat and blood triglyceride in Chinese hypertriglyceridemic subjects. European Journal of Clinical Nutrition 63, 879-886.
50. Van den Bossche, J., Baardman, J., Otto, N. A., van der Velden, S., Neele, A. E., van den Berg, S. M., Luque-Martin, R., Chen, H.-J., Boshuizen, M. C., Ahmed, M. (2016) Mitochondrial dysfunction prevents repolarization of inflammatory macrophages. Cell reports 17, 684-696.
51. He, L., Weber, K., Schilling, J. (2016) Glutamine modulates macrophage lipotoxicity. Nutrients 8, 215.
52. Chong, J., Wishart, D. S., Xia, J. (2019) Using MetaboAnalyst 4.0 for Comprehensive and Integrative Metabolomics Data Analysis. Current Protocols in Bioinformatics 68, e86.

53. Wiklund, S., Johansson, E., Sjöström, L., Mellerowicz, E. J., Edlund, U., Shockcor, J. P., Gottfries, J., Moritz, T., Trygg, J. (2008) Visualization of GC/TOF-MS-Based Metabolomics Data for Identification of Biochemically Interesting Compounds Using OPLS Class Models. Analytical Chemistry 80, 115-122.
54. Tomfohr, J., Lu, J., Kepler, T. B. (2005) Pathway level analysis of gene expression using singular value decomposition. BMC bioinformatics 6, 225-225.
55. Mudunuri, U., Che,A., Yi,M. and Stephens,R.M (2009) bioDBnet: the biological database network. Bioinformatics 25, 2.
56. Huang, D. W., Sherman, B. T., Lempicki, R. A. (2009) Systematic and integrative analysis of large gene lists using DAVID bioinformatics resources. Nature Protocols 4, 44-57.
57. Huang, D. W., Sherman, B. T., Lempicki, R. A. (2008) Bioinformatics enrichment tools: paths toward the comprehensive functional analysis of large gene lists. Nucleic acids research 37, 1-13.
58. Ambarus, C. A., Krausz, S., van Eijk, M., Hamann, J., Radstake, T. R. D. J., Reedquist, K. A., Tak, P. P., Baeten, D. L. P. (2012) Systematic validation of specific phenotypic markers for in vitro polarized human macrophages. Journal of Immunological Methods 375, 196-206.
59. Gause, W. C., Wynn, T. A., Allen, J. E. (2013) Type 2 immunity and wound healing: evolutionary refinement of adaptive immunity by helminths. Nature Reviews Immunology 13, 607.
60. Dinarello, C. A. (2018) Overview of the IL-1 family in innate inflammation and acquired immunity. Immunol Rev 281, 8-27.
61. Santarlasci, V., Cosmi, L., Maggi, L., Liotta, F., Annunziato, F. (2013) IL-1 and T Helper Immune Responses. Frontiers in immunology 4, 182-182.
62. Hurst, S. M., Wilkinson, T. S., McLoughlin, R. M., Jones, S., Horiuchi, S., Yamamoto, N., Rose-John, S., Fuller, G. M., Topley, N., Jones, S. A. (2001) IL-6 and Its Soluble Receptor Orchestrate a Temporal Switch in the Pattern of Leukocyte Recruitment Seen during Acute Inflammation. Immunity 14, 705-714.
63. Lee, S. H., Kwon, J. y., Kim, S.-Y., Jung, K., Cho, M.-L. (2017) Interferon-gamma regulates inflammatory cell death by targeting necroptosis in experimental autoimmune arthritis. Scientific Reports 7, 10133.
64. Langlais, D., Barreiro, L. B., Gros, P. (2016) The macrophage IRF8/IRF1 regulome is required for protection against infections and is associated with chronic inflammation. The Journal of experimental medicine 213, 585-603.
65. Sudan, B., Wacker, M. A., Wilson, M. E., Graff, J. W. (2015) A systematic approach to identify markers of distinctly activated human macrophages. Frontiers in Immunology 6, 18.
66. Katakura, T., Miyazaki, M., Kobayashi, M., Herndon, D. N., Suzuki, F. (2004) CCL17 and IL-10 as Effectors That Enable Alternatively Activated Macrophages to Inhibit the Generation of Classically Activated Macrophages. The Journal of Immunology 172, 1407.
67. Wilkinson, H. N., Roberts, E. R., Stafford, A. R., Banyard, K. L., Matteucci, P., Mace, K. A., Hardman, M. J. (2019) Tissue Iron Promotes Wound Repair via M2 Macrophage Polarization and the Chemokine (C-C Motif) Ligands 17 and 22. The American journal of pathology 189, 2196-2208.
68. Boxx, G. M. and Cheng, G. (2016) The Roles of Type I Interferon in Bacterial Infection. Cell host & microbe 19, 760-769.
69. Philippidis, P., Mason, J., Evans, B., Nadra, I., Taylor, K., Haskard, D., Landis, R. (2004) Hemoglobin scavenger receptor CD163 mediates interleukin-10 release and heme oxygenase-1 synthesis: antiinflammatory monocyte-macrophage responses in vitro, in resolving skin blisters in vivo, and after cardiopulmonary bypass surgery. Circulation research 94, 119-126.
70. Cai, B., Kasikara, C., Doran, A. C., Ramakrishnan, R., Birge, R. B., Tabas, I. (2018) MerTK signaling in macrophages promotes the synthesis of inflammation resolution mediators by suppressing CaMKII activity. Science Signaling 11, eaar3721.
71. Wang, Q., Ni, H., Lan, L., Wei, X., Xiang, R., Wang, Y. (2010) Fra-1 protooncogene regulates IL-6 expression in macrophages and promotes the generation of M2d macrophages. Cell research 20, 701.
72. Munn, D. H., Shafizadeh, E., Attwood, J. T., Bondarev, I., Pashine, A., Mellor, A. L. (1999) Inhibition of T cell proliferation by macrophage tryptophan catabolism. The Journal of experimental medicine 189, 1363-1372.
73. Balce, D. R. and Yates, R. M. (2013) Redox-sensitive probes for the measurement of redox chemistries within phagosomes of macrophages and dendritic cells. Redox Biology 1, 467-474.

74. Ji, L., Zhao, X., Zhang, B., Kang, L., Song, W., Zhao, B., Xie, W., Chen, L., Hu, X. (2019) Slc6a8-Mediated Creatine Uptake and Accumulation Reprogram Macrophage Polarization via Regulating Cytokine Responses. Immunity 51, 272-284.e7.
75. Papathanassiu, A. E., Ko, J.-H., Imprialou, M., Bagnati, M., Srivastava, P. K., Vu, H. A., Cucchi, D., McAdoo, S. P., Ananieva, E. A., Mauro, C. (2017) BCAT1 controls metabolic reprogramming in activated human macrophages and is associated with inflammatory diseases. Nature communications 8, 16040.
76. Fritsche, K. L. (2015) The science of fatty acids and inflammation. Adv Nutr 6, 293S-301S.
77. Camell, C. D., Nguyen, K. Y., Jurczak, M. J., Christian, B. E., Shulman, G. I., Shadel, G. S., Dixit, V. D. (2015) Macrophage-specific de Novo Synthesis of Ceramide Is Dispensable for Inflammasome-driven Inflammation and Insulin Resistance in Obesity. The Journal of biological chemistry 290, 29402-29413.
78. Gough, N. R. (2014) Inhibiting HIF with Fructose-1,6-Bisphosphastase. Science Signaling 7, ec253.
79. Qadri, M., Almadani, S., Jay, G. D., Elsaid, K. A. (2018) Role of CD44 in Regulating TLR2 Activation of Human Macrophages and Downstream Expression of Proinflammatory Cytokines. Journal of immunology (Baltimore, Md. : 1950) 200, 758-767.
80. Tamada, M., Nagano, O., Tateyama, S., Ohmura, M., Yae, T., Ishimoto, T., Sugihara, E., Onishi, N., Yamamoto, T., Yanagawa, H., Suematsu, M., Saya, H. (2012) Modulation of Glucose Metabolism by CD44 Contributes to Antioxidant Status and Drug Resistance in Cancer Cells. Cancer research 72, 1438.
81. Di Virgilio, F. and Adinolfi, E. (2017) Extracellular purines, purinergic receptors and tumor growth. Oncogene 36, 293-303.
82. Matsuzawa, A. (2017) Thioredoxin and redox signaling: Roles of the thioredoxin system in control of cell fate. Archives of Biochemistry and Biophysics 617, 101-105.
83. Sorgi, C. A., Zarini, S., Martin, S. A., Sanchez, R. L., Scandiuzzi, R. F., Gijón, M. A., Guijas, C., Flamand, N., Murphy, R. C., Faccioli, L. H. (2017) Dormant 5-lipoxygenase in inflammatory macrophages is triggered by exogenous arachidonic acid. Scientific Reports 7, 10981.
84. Serhan, C. N. and Levy, B. D. (2018) Resolvins in inflammation: emergence of the pro-resolving superfamily of mediators. The Journal of Clinical Investigation 128, 2657-2669.
85. Camell, C. D., Nguyen, K. Y., Jurczak, M. J., Christian, B. E., Shulman, G. I., Shadel, G. S., Dixit, V. D. (2015) Macrophage-specific de novo synthesis of ceramide is dispensable for inflammasome-driven inflammation and insulin resistance in obesity. Journal of Biological Chemistry 290, 29402-29413.
86. Fucho, R., Casals, N., Serra, D., Herrero, L. (2016) Ceramides and mitochondrial fatty acid oxidation in obesity. The FASEB Journal 31, 1263-1272.
87. Kogot-Levin, A. and Saada, A. (2014) Ceramide and the mitochondrial respiratory chain. Biochimie 100, 88-94.
88. Kämpfer, H., Schmidt, R., Geisslinger, G., Pfeilschifter, J., Frank, S. (2005) Wound Inflammation in Diabetic ob/ob Mice. Diabetes 54, 1543.
89. Lefèvre, L., Galès, A., Olagnier, D., Bernad, J., Perez, L., Burcelin, R., Valentin, A., Auwerx, J., Pipy, B., Coste, A. (2010) PPARγ ligands switched high fat diet-induced macrophage M2b polarization toward M2a thereby improving intestinal Candida elimination. PloS one 5, e12828-e12828.
90. Rattigan, K. M., Pountain, A. W., Regnault, C., Achcar, F., Vincent, I. M., Goodyear, C. S., Barrett, M. P. (2018) Metabolomic profiling of macrophages determines the discrete metabolomic signature and metabolomic interactome triggered by polarising immune stimuli. PloS one 13.
91. Meiser, J., Krämer, L., Sapcariu, S. C., Battello, N., Ghelfi, J., D'Herouel, A. F., Skupin, A., Hiller, K. (2016) Pro-inflammatory Macrophages Sustain Pyruvate Oxidation through Pyruvate Dehydrogenase for the Synthesis of Itaconate and to Enable Cytokine Expression. Journal of Biological Chemistry 291, 3932-3946.
92. Wang, F., Zhang, S., Vuckovic, I., Jeon, R., Lerman, A., Folmes, C. D., Dzeja, P. P., Herrmann, J. (2018) Glycolytic Stimulation Is Not a Requirement for M2 Macrophage Differentiation. Cell Metabolism 28, 463-475.e4.
93. Curran, J. N., Winter, D. C., Bouchier-Hayes, D. (2006) Biological fate and clinical implications of arginine metabolism in tissue healing. Wound Repair and Regeneration 14, 376-386.
94. Nishiyama, A., Yokote, Y., Sakagami, H. (2010) Changes in Amino Acid Metabolism During Activation of Mouse Macrophage-like Cell Lines. In Vivo 24, 857-860.

Figure Legends

Figure 1: Macrophage Functional Phenotyping by Common Cell-Surface Markers. Cell surface marker profile of six MΦ phenotypes harvested at 72 hours post polarization were detected by FACS. CD14+ monocytes were isolated from human blood-derived PBMCs, differentiated into resting MΦ (M0, shown in blue) with M-CSF ex vivo, and polarized into five activated phenotypes using IFN-γ/LPS (M1, shown in red), IL-4/IL-13 (M2a, shown in yellow), IC/LPS (M2b, shown in green), IL-10 (M2c, shown in gray), or IL-6/LIF (M2d, shown in purple). FACS gating on four common MΦ cell surface markers for all six MΦ phenotypes is shown as live cell count for each marker gate **(A-D)** and mean fluorescence intensity (MFI) profile of gate **(E-H)**. CD40 co-stimulatory protein of APCs is prominently displayed on classically activated, pro-inflammatory MΦ (M1) **(A, E)**. CD86 co-stimulatory protein indicates prominent display on alternately activated, anti-inflammatory MΦ (M2a) and M1 MΦ **(B, F)**. CD163 bacterial pathogen sensor is displayed on resting MΦ (M0), alternately activated tissue repair MΦ (M2c), and tumor associated MΦ (M2d) **(C, G)**. HLA-DR MHC class II receptor is displayed on all phenotypes except the alternately activated tissue-remodeling MΦ (M2b) **(D, H)**. Histograms are total cell count and representative of three biological replicates. MFI is normalized to

Figure 2: Macrophage Functional Phenotyping by Gene and Protein Expression of Immunomodulatory Factors. Multiplex detection of immunomodulatory factors in six MΦ phenotypes were detected using magnetic bead-based quantification of mRNA and secreted protein. CD14+ monocytes were isolated from human blood-derived PBMCs, differentiated into resting MΦ (M0, shown in blue) with M-CSF *ex vivo*, and polarized into five activated phenotypes using IFN-γ/LPS (M1, shown in red), IL-4/IL-13 (M2a, shown in yellow), IC/LPS (M2b, shown in green), IL-10 (M2c, shown in gray), or IL-6/LIF (M2d, shown in purple). Gene and protein expression profile (diamond-whisker plots and bar charts, respectively) of key functional molecules were profiled by multiplex assay after 24 hrs of *ex vivo* polarization. Immunomodulatory function includes pro-inflammatory (TNFα, IL-12p70, CCL3, CXCL10, CXCL8, and IFNα) **(A)**, immune-regulatory/tissue-repair (IL-10, IL-6, IL-1b, IL-1α, TGF-b, and CCL2) **(B)**, and growth factors (GM-CSF, PDGF-BB, and VEGF-A) **(C)**. Diamond-whisker plots display 25%-75% quartile range, median, and mean. Bar charts indicate mean ± SEM. Expression profiles were normalized to total cell count and include three biological replicates (N=3).

Figure 3: Macrophage Polarization into Functional Phenotypes Activates Distinct Gene Expression Profiles Relative to the Parent, Resting Macrophage Phenotype (M0). Gene set enrichment analysis (GSEA) and pathway impact scoring of global myeloid gene expression demonstrates distinct patterns in five polarized MΦ phenotypes. Briefly, multiplexed myeloid gene expression was directly detected through molecular barcode probes and normalized to the geometric mean of the housekeeping gene set. GSEA for each phenotype was calculated for pathway impact relative to the non-polarized, resting MΦ (M0). Radar plots for each polarized MΦ phenotype display pathway score based on impact regardless of whether genes were up- or down-regulated (Undirected Global Significance [UGS], solid color) and pathway score based on impact incorporating t-statistic comparison of gene regulation as relatively increased or decreased (Directed Global Significance [DGS], hatch marks). Radar plots include UGS and DGS scores for all five polarized MΦ phenotypes: M1 MΦs (IFN-γ/LPS treated, shown in red) **(A)**, M2a MΦs (IL-4/IL-13 treated, shown in yellow) **(B)**, M2b MΦs (IC/LPS treated, shown in green) **(C)**, M2c MΦs (IL-10 treated, shown in gray) **(D)**, and M2d MΦs (IL-6/LIF treated, shown in purple) **(E)**. GSEA based on three experimental replicates for each MΦ s phenotype (N=3).

Figure 4: Gene Expression Profile Comparison of Polarized Macrophage Phenotypes Identifies Unique and Overlapping Immunomodulatory Functions. Gene Ontology (GO) annotation of global myeloid gene expression in five MΦ phenotypes identifies relative biological functionality across polarized states. Multiplexed myeloid gene expression profile of all five polarized MΦ phenotypes was used to annotate impacted biological functionality based on GO Processes. For each MΦ phenotype, the top 15 impacted GO processes significantly enriched ($p \leq 0.05$) were plotted relative to the other four polarized MΦ phenotypes. Enrichment plots for prioritized GO process profile include all five polarized MΦ phenotypes: M1 MΦs (IFN-γ/LPS treated, shown in red) **(A)**, M2a MΦs (IL-4/IL-13 treated, shown in yellow) **(B)**, M2b MΦs (IC/LPS treated, shown in green) **(C)**, M2c MΦs (IL-10 treated, shown in gray) **(D)**, and M2d MΦs (IL-6/LIF treated, shown in purple) **(E)**. GO process annotation was based on three experimental replicates for each MΦ s phenotype (N=3).

Figure 5: Untargeted Metabolomics of Five Polarized Macrophage Phenotypes Identifies Biomarkers of Shared and Unique Profile Relative to the Parent, Resting Macrophage Phenotype. Global metabolomics profile of the parent, resting MΦ phenotype (M0) and five polarized MΦ phenotypes identified 498 compounds of known identity, normalized to cell count. MΦ metabotype clustering was determined through Orthogonal Projections to Latent Structures Discriminant Analysis (OPLS-DA), inset clustering scores plots with 2D T-scores **(A.1, B.1, C.1, D.1, & E.1)**. S-plot comparison of each polarized MΦ phenotype was plotted relative to the resting, parent MΦ phenotype (denoted in blue) **(A.1, B.1, C.1, D.1, & E.1)** and normalized peak intensity for biomarkers of particular note **(a, b, c)** are displayed as box-whisker plots **(A.2, B.2, C.2, D.2, & E.2)**. Multivariate, cluster analysis is displayed for all five polarized MΦ phenotypes: M1 MΦs (IFN-γ/LPS treated, shown in red) **(A)**, M2a MΦs (IL-4/IL-13 treated, shown in yellow) **(B)**, M2b MΦs (IC/LPS treated, shown in green) **(C)**, M2c MΦs (IL-10 treated, shown in gray) **(D)**, and M2d MΦs (IL-6/LIF treated, shown in purple) **(E)**. Untargeted metabolomics profiles are based on three experimental replicates for each MΦ phenotype (N=3).

Figure 6: Global Metabolomics Comparison of the Classically Activated Macrophage Phenotype (M1 MΦ) to Four Subtypes of Alternately Activated Macrophage Phenotypes (M2a, M2b, M2c, & M2d MΦ). OPLS-DA clustering relative to the parent, resting MΦ phenotype (M0 MΦ) identified metabolite biomarkers correlated with all five polarized MΦ phenotypes based on OPLS-DA variable influence on projection (VIP) values. VIP values were used to identified both shared and unique metabolite biomarkers of the classically-activated M1 MΦ phenotype and four subtypes of the alternately-activated M2 MΦ phenotypes, displayed as OPLS-DA Shared and Unique Structures (SUS) plots (A.1, B.1, C.1, and D.1). For each SUS plot, metabolite biomarkers uniquely correlated to the M1 MΦ phenotype (red diamonds) are plotted along the x-axis and those metabolite biomarkers uniquely correlated to the M2 MΦ phenotype are plotted along the y-axis. Shared metabolite biomarkers (black circles) are plotted along the diagonals, reflecting biomarker positive/negative correlation to each polarized MΦ phenotype relative to the parent, resting MΦ phenotype (M0 MΦ). Associated biomarkers and correlation scores are shown in matching tables (A.2, B.2, C.2, and D.2). OPLS-DA SUS plots are displayed for four polarized M2 MΦ phenotypes, relative to the M1 MΦs (IFN-γ/LPS treated, shown in red): M2a MΦs (IL-4/IL-13 treated, shown in yellow) (A), M2b MΦs (IC/LPS treated, shown in green) (B), M2c MΦs (IL-10 treated, shown in gray) (C), and M2d MΦs (IL-6/LIF treated, shown in purple) (D). Untargeted metabolomics profiles are based on three experimental replicates for each MΦ phenotype (N=3).

Figure 7: Metabotype Profiling of Polarized Macrophages. Untargeted, global metabolomics profile of polarized MΦ phenotypes identified 498 known compounds, normalized to total cell count, and profiled relative to the resting M0 MΦ phenotype. For normalized, M0-relative metabolite profiles, over-representation analysis by hypergeometric testing and pathway topology analysis by two node centrality measures (degree centrality and betweenness centrality) was performed for each polarized MΦ phenotype including M1 MΦs (IFN-γ/LPS treated, shown in red) (A), M2a MΦs (IL-4/IL-13 treated, shown in yellow) (B), M2b MΦs (IC/LPS treated, shown in green) (C), M2c MΦs (IL-10 treated, shown in gray) (D), and M2d MΦs (IL-6/LIF treated, shown in purple) (E). Metabolic Pathway Topology is plotted as Pathway Impact (x-axis) and significance of pathway topography (-Log [p value], y-axis) for each polarized MΦ phenotype.

Figure 8: Macrophage Polarization into Functional Phenotypes Activates Distinct Metabolic Gene Expression Profiles Relative to the Parent, Resting Macrophage Phenotype (M0). Gene set enrichment analysis (GSEA) and pathway impact scoring of global myeloid gene expression demonstrates distinct patterns in metabolism-related transcripts in the five polarized MΦ phenotypes. Associated metabolism gene expression profiles for most impacted pathways are shown including A) central metabolism, B) amino acid metabolism, C) fatty acid metabolism, D) arachidonic acid metabolism, and E) miscellaneous pathways. Red bars represent gene targets that are differentially regulated ($p \leq 0.05$) when compared to the M0 phenotype. Myeloid gene expression was directly detected through molecular barcode probes and normalized to the geometric mean of the housekeeping gene set. Gene expression is mean ± SEM. Pathway topology and metabolic gene expression profiles are based on triplicate, experimental replicates (N=3).

Figure 9:

Figures

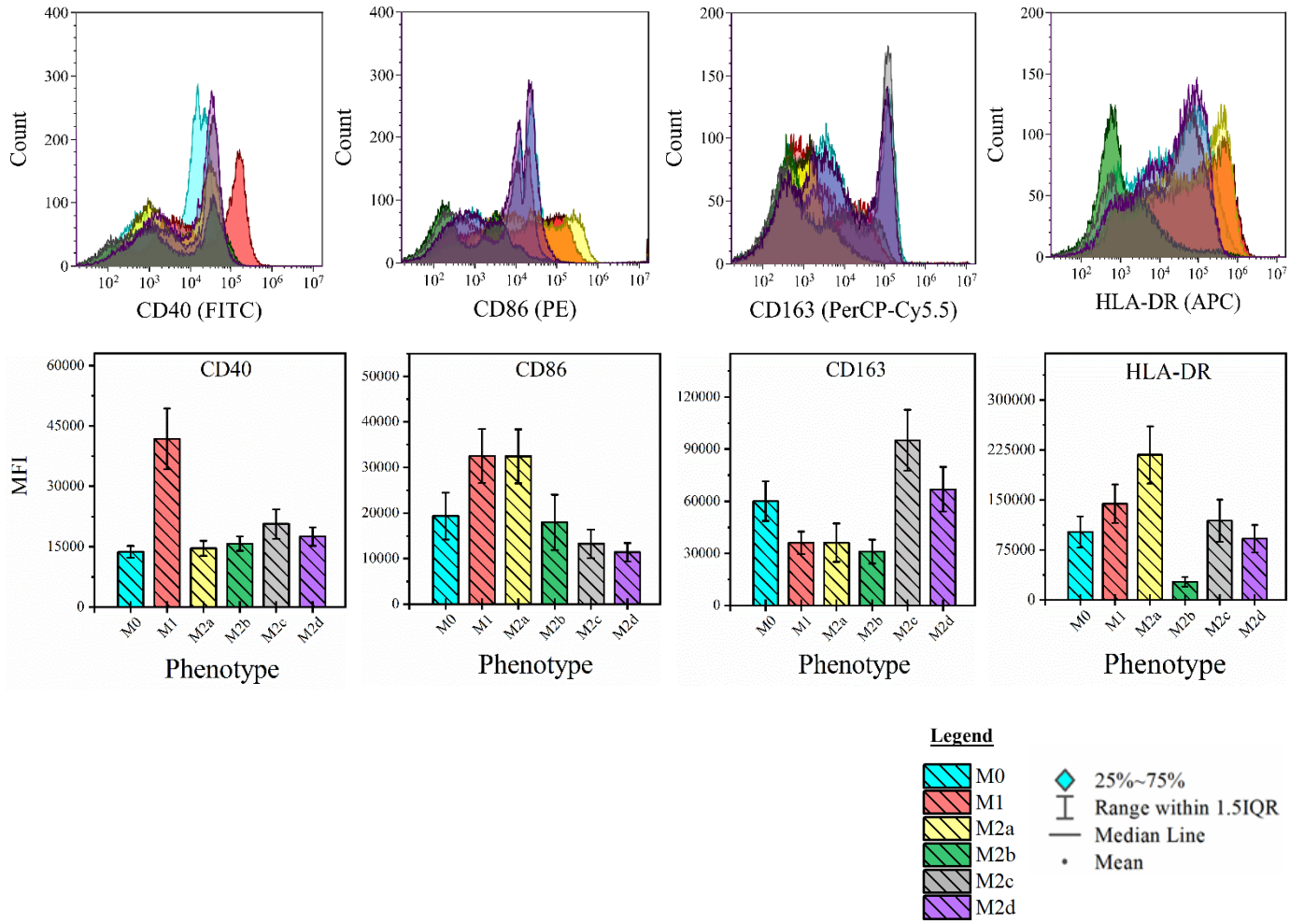

Figure 1: Macrophage Functional Phenotyping by Common Cell-Surface Markers. Cell surface marker profile of six MΦ phenotypes harvested at 72 hours post polarization were detected by FACS. CD14+ monocytes were isolated from human blood-derived PBMCs, differentiated into resting MΦ (M0, shown in blue) with M-CSF ex vivo, and polarized into five activated phenotypes using IFN-γ/LPS (M1, shown in red), IL-4/IL-13 (M2a, shown in yellow), IC/LPS (M2b, shown in green), IL-10 (M2c, shown in gray), or IL-6/LIF (M2d, shown in purple). FACS gating on four common MΦ cell surface markers for all six MΦ phenotypes is shown as live cell count for each marker gate **(A-D)** and mean fluorescence intensity (MFI) profile of gate **(E-H)**. CD40 co-stimulatory protein of APCs is prominently displayed on classically activated, pro-inflammatory MΦ (M1) **(A, E)**. CD86 co-stimulatory protein indicates prominent display on alternately activated, anti-inflammatory MΦ (M2a) and M1 MΦ **(B, F)**. CD163 bacterial pathogen sensor is displayed on resting MΦ (M0), alternately activated tissue repair MΦ (M2c), and tumor associated MΦ (M2d) **(C, G)**. HLA-DR MHC class II receptor is displayed on all phenotypes except the alternately activated tissue-remodeling MΦ (M2b) **(D, H)**. Histograms are total cell count and representative of three biological replicates. MFI is normalized to total cell count and includes all three biological replicates (N=3, mean ± SEM).

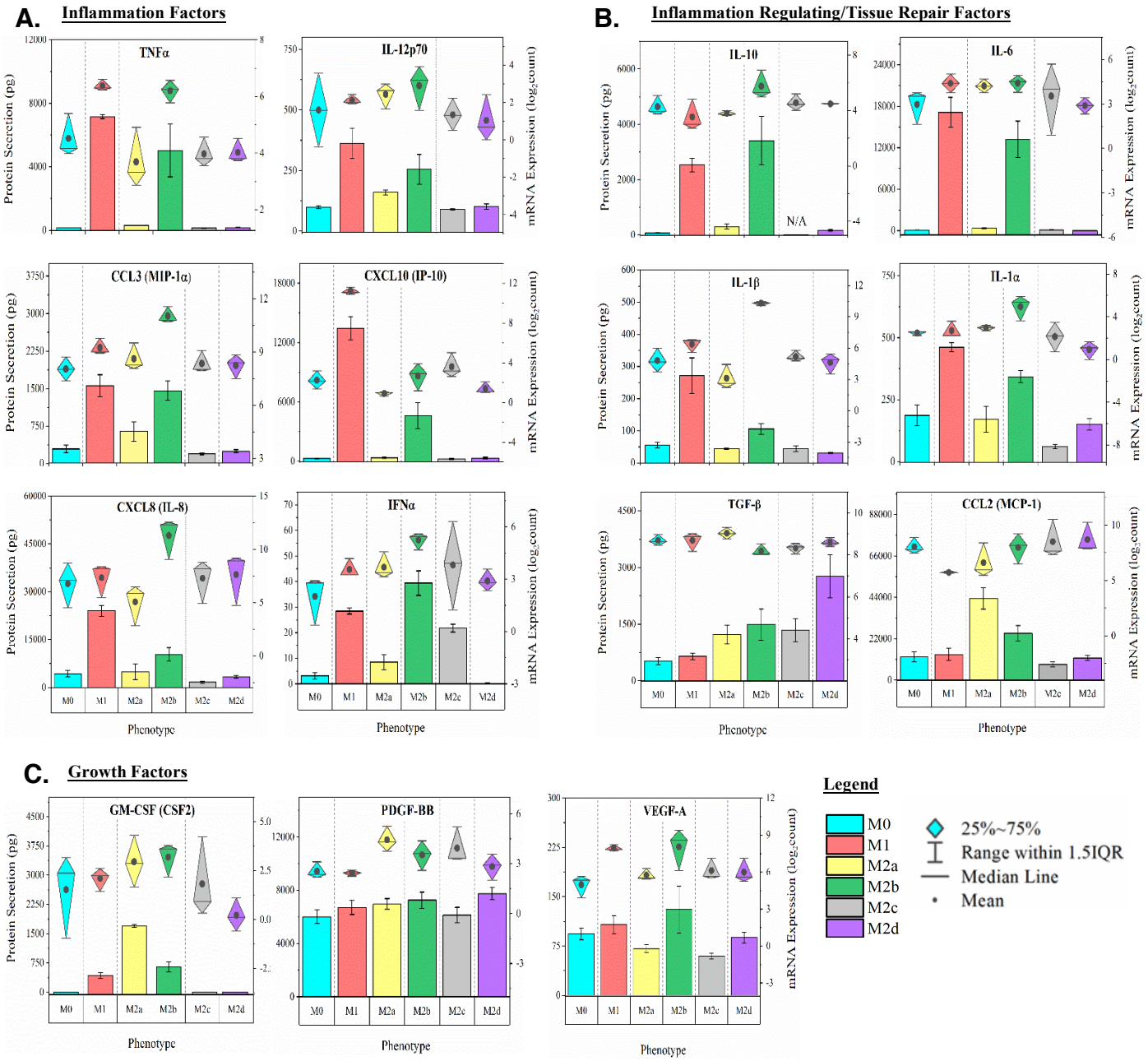

Figure 2: Macrophage Functional Phenotyping by Gene and Protein Expression of Immunomodulatory Factors. Multiplex detection of immunomodulatory factors in six MΦ phenotypes were detected using magnetic bead-based quantification of mRNA and secreted protein. CD14+ monocytes were isolated from human blood-derived PBMCs, differentiated into resting MΦ (M0, shown in blue) with M-CSF *ex vivo*, and polarized into five activated phenotypes using IFN-γ/LPS (M1, shown in red), IL-4/IL-13 (M2a, shown in yellow), IC/LPS (M2b, shown in green), IL-10 (M2c, shown in gray), or IL-6/LIF (M2d, shown in purple). Gene and protein expression profile (diamond-whisker plots and bar charts, respectively) of key functional molecules were profiled by multiplex assay after 24 hrs of *ex vivo* polarization. Immunomodulatory function includes pro-inflammatory (TNFα, IL-12p70, CCL3, CXCL10, CXCL8, and IFNα) **(A)**, immune-regulatory/tissue-repair (IL-10, IL-6, IL-1b, IL-1α, TGF-b, and CCL2) **(B)**, and growth factors (GM-CSF, PDGF-BB, and VEGF-A) **(C)**. Diamond-whisker plots display 25%-75% quartile range, median, and mean. Bar charts indicate mean ± SEM. Expression profiles were normalized to total cell count and include three biological replicates (N=3).

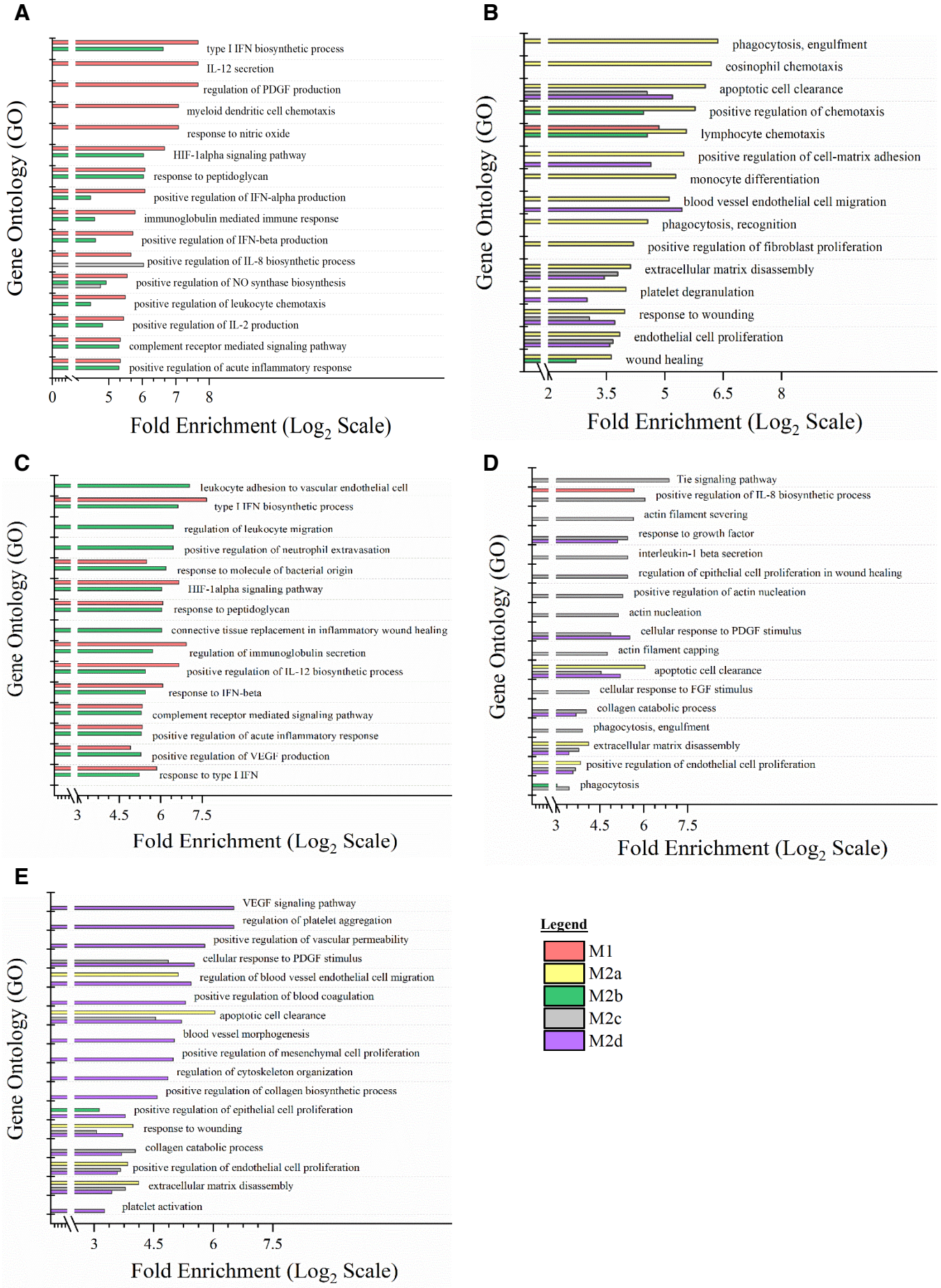
A
Gene Ontology (GO)
type I IFN biosynthetic process
IL-12 secretion
regulation of PDGF production
myeloid dendritic cell chemotaxis
response to nitric oxide
HIF-1alpha signaling pathway
response to peptidoglycan
positive regulation of IFN-alpha production
immunoglobulin mediated immune response
positive regulation of IFN-beta production
positive regulation of IL-8 biosynthetic process
positive regulation of NO synthase biosynthesis
positive regulation of leukocyte chemotaxis
positive regulation of IL-2 production
complement receptor mediated signaling pathway
positive regulation of acute inflammatory response
0 5 6 7 8
Fold Enrichment (Log2 Scale)
B
Gene Ontology (GO)
phagocytosis, engulfment
eosinophil chemotaxis
apoptotic cell clearance
positive regulation of chemotaxis
lymphocyte chemotaxis
positive regulation of cell-matrix adhesion
monocyte differentiation
blood vessel endothelial cell migration
phagocytosis, recognition
positive regulation of fibroblast proliferation
extracellular matrix disassembly
platelet degranulation
response to wounding
endothelial cell proliferation
wound healing
2 3.5 5 6.5 8
Fold Enrichment (Log2 Scale)
C
Gene Ontology (GO)
leukocyte adhesion to vascular endothelial cell
type I IFN biosynthetic process
regulation of leukocyte migration
positive regulation of neutrophil extravasation
response to molecule of bacterial origin
HIF-1alpha signaling pathway
response to peptidoglycan
connective tissue replacement in inflammatory wound healing
regulation of immunoglobulin secretion
positive regulation of IL-12 biosynthetic process
response to IFN-beta
complement receptor mediated signaling pathway
positive regulation of acute inflammatory response
positive regulation of VEGF production
response to type I IFN
3 4.5 6 7.5
Fold Enrichment (Log2 Scale)
D
Gene Ontology (GO)
Tie signaling pathway
positive regulation of IL-8 biosynthetic process
actin filament severing
response to growth factor
interleukin-1 beta secretion
regulation of epithelial cell proliferation in wound healing
positive regulation of actin nucleation
actin nucleation
cellular response to PDGF stimulus
actin filament capping
apoptotic cell clearance
cellular response to FGF stimulus
collagen catabolic process
phagocytosis, engulfment
extracellular matrix disassembly
positive regulation of endothelial cell proliferation
phagocytosis
3 4.5 6 7.5
Fold Enrichment (Log2 Scale)
E
Gene Ontology (GO)
VEGF signaling pathway
regulation of platelet aggregation
positive regulation of vascular permeability
cellular response to PDGF stimulus
regulation of blood vessel endothelial cell migration
positive regulation of blood coagulation
apoptotic cell clearance
blood vessel morphogenesis
positive regulation of mesenchymal cell proliferation
regulation of cytoskeleton organization
positive regulation of collagen biosynthetic process
positive regulation of epithelial cell proliferation
response to wounding
collagen catabolic process
positive regulation of endothelial cell proliferation
extracellular matrix disassembly
platelet activation
3 4.5 6 7.5
Fold Enrichment (Log2 Scale)
Legend
M1
M2a
M2b
M2c
M2d

Figure 3: Macrophage Polarization into Functional Phenotypes Activates Distinct Gene Expression Profiles Relative to the Parent, Resting Macrophage Phenotype (M0). Gene set enrichment analysis (GSEA) and pathway impact scoring of global myeloid gene expression demonstrates distinct patterns in five polarized MΦ phenotypes. Briefly, multiplexed myeloid gene expression was directly detected through molecular barcode probes and normalized to the geometric mean of the housekeeping gene set. GSEA for each phenotype was calculated for pathway impact relative to the non-polarized, resting MΦ (M0). Radar plots for each polarized MΦ phenotype display pathway score based on impact regardless of whether genes were up- or down-regulated (Undirected Global Significance [UGS], solid color) and pathway score based on impact incorporating t-statistic comparison of gene regulation as relatively increased or decreased (Directed Global Significance [DGS], hatch marks). Radar plots include UGS and DGS scores for all five polarized MΦ phenotypes: M1 MΦs (IFN-γ/LPS treated, shown in red) **(A)**, M2a MΦs (IL-4/IL-13 treated, shown in yellow) **(B)**, M2b MΦs (IC/LPS treated, shown in green) **(C)**, M2c MΦs (IL-10 treated, shown in gray) **(D)**, and M2d MΦs (IL-6/LIF treated, shown in purple) **(E)**. GSEA based on three experimental replicates for each MΦ s phenotype (N=3).

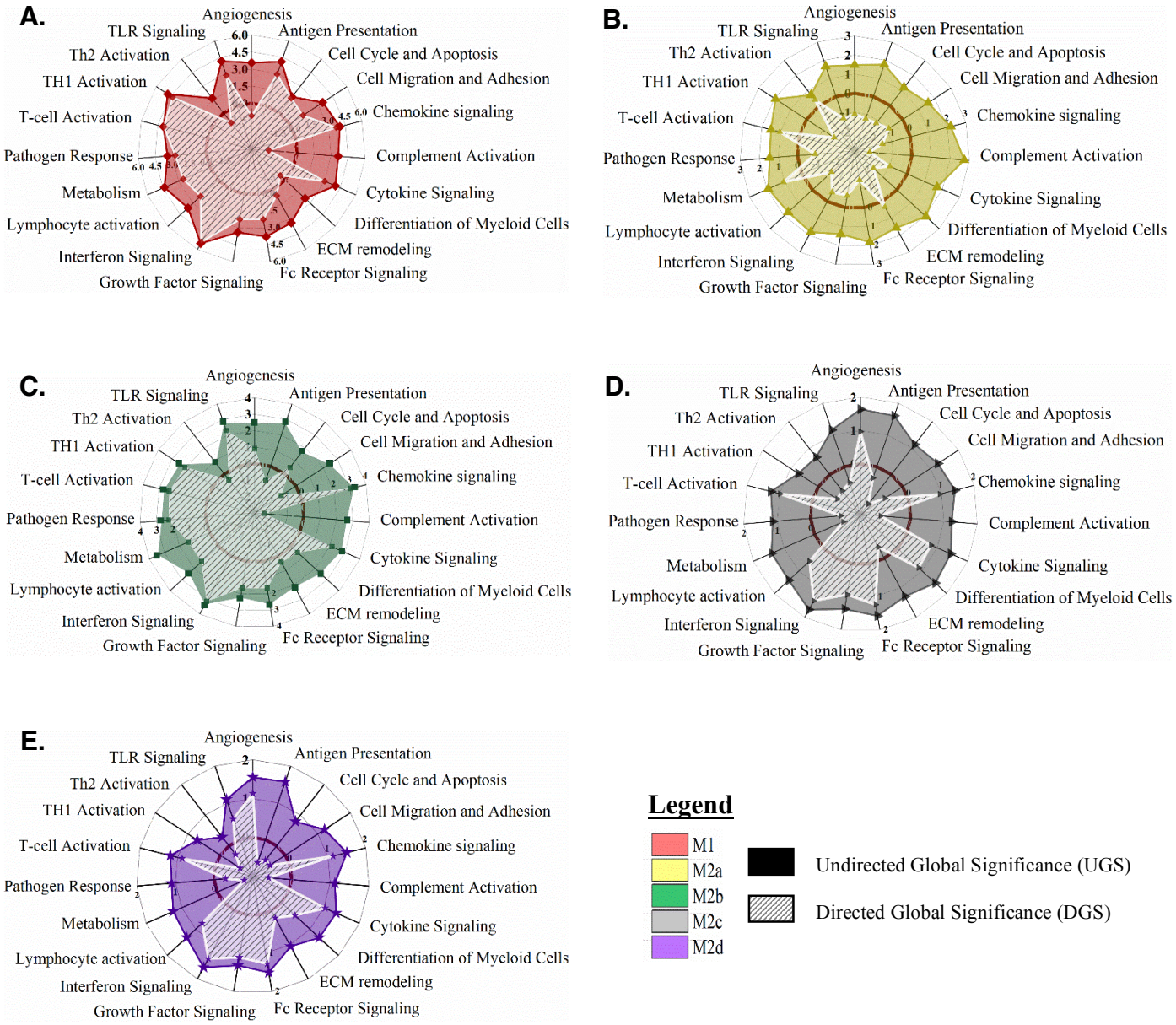

Figure 4: Gene Expression Profile Comparison of Polarized Macrophage Phenotypes Identifies Unique and Overlapping Immunomodulatory Functions. Gene Ontology (GO) annotation of global myeloid gene expression in five MΦ phenotypes identifies relative biological functionality across polarized states. Multiplexed myeloid gene expression profile of all five polarized MΦ phenotypes was used to annotate impacted biological functionality based on GO Processes. For each MΦ phenotype, the top 15 impacted GO processes significantly enriched ($p \leq 0.05$) were plotted relative to the other four polarized MΦ phenotypes. Enrichment plots for prioritized GO process profile include all five polarized MΦ phenotypes: M1 MΦs (IFN-γ/LPS treated, shown in red) **(A)**, M2a MΦs (IL-4/IL-13 treated, shown in yellow) **(B)**, M2b MΦs (IC/LPS treated, shown in green) **(C)**, M2c MΦs (IL-10 treated, shown in gray) **(D)**, and M2d MΦs (IL-6/LIF treated, shown in purple) **(E)**. GO process annotation was based on three experimental replicates for each MΦ s phenotype (N=3).

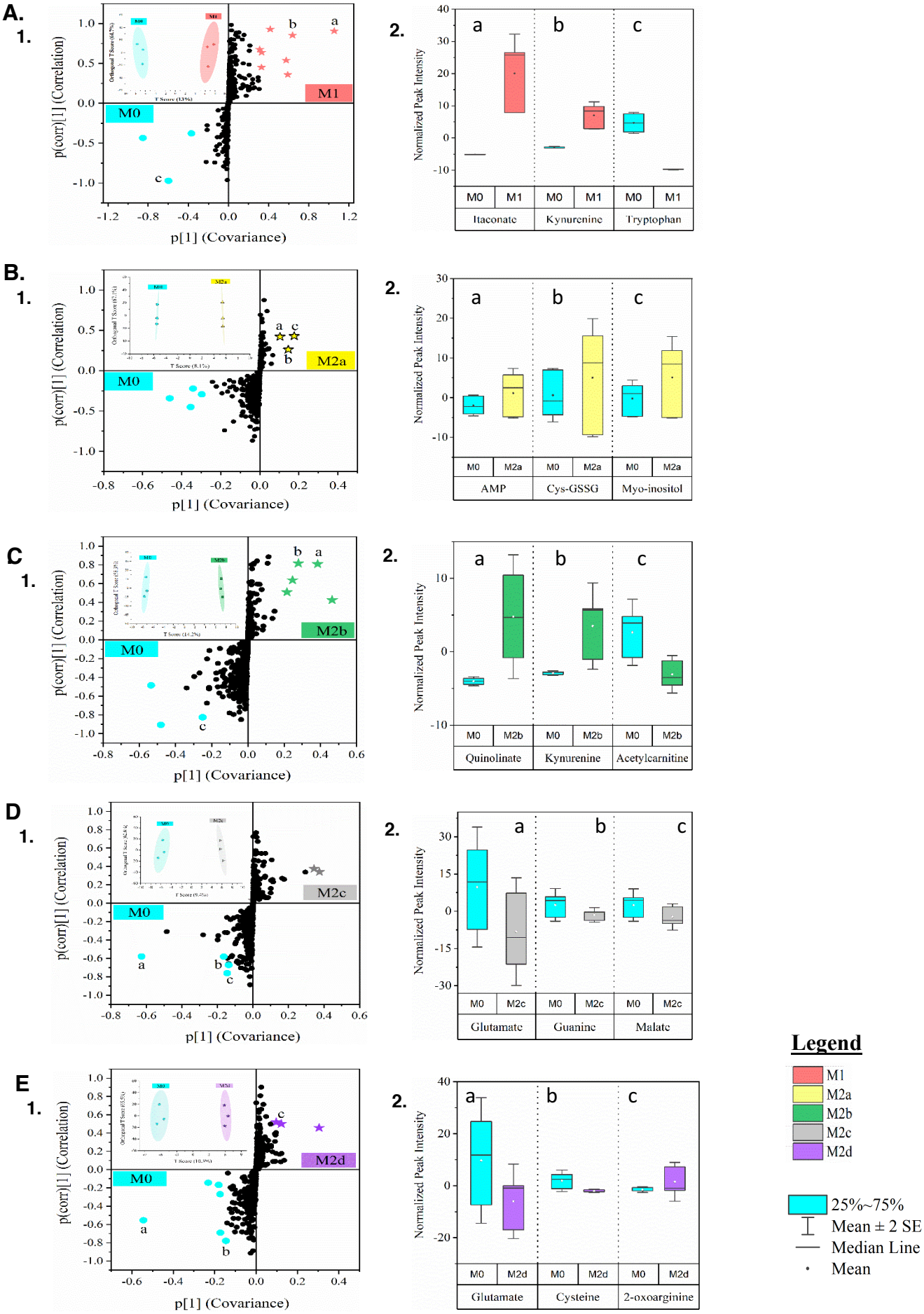
A.
1.
M0
M1
p(corr)[1] (Correlation)
p[1] (Covariance)
2.
Normalized Peak Intensity
Itaconate
Kynurenine
Tryptophan
B.
1.
M0
M2a
2.
AMP
Cys-GSSG
Myo-inositol
C
1.
M0
M2b
2.
Quinolinate
Kynurenine
Acetylcarnitine
D
1.
M0
M2c
2.
Glutamate
Guanine
Malate
E
1.
M0
M2d
2.
Glutamate
Cysteine
2-oxoarginine
Legend
M1
M2a
M2b
M2c
M2d
25%~75%
Mean ± 2 SE
Median Line
Mean

Figure 5: Untargeted Metabolomics of Five Polarized Macrophage Phenotypes Identifies Biomarkers of Shared and Unique Profile Relative to the Parent, Resting Macrophage Phenotype. Global metabolomics profile of the parent, resting MΦ phenotype (M0) and five polarized MΦ phenotypes identified 498 compounds of known identity, normalized to cell count. MΦ metabotype clustering was determined through Orthogonal Projections to Latent Structures Discriminant Analysis (OPLS-DA), inset clustering scores plots with 2D T-scores **(A.1, B.1, C.1, D.1, & E.1)**. S-plot comparison of each polarized MΦ phenotype was plotted relative to the resting, parent MΦ phenotype (denoted in blue) **(A.1, B.1, C.1, D.1, & E.1)** and normalized peak intensity for biomarkers of particular note **(a, b, c)** are displayed as box-whisker plots **(A.2, B.2, C.2, D.2, & E.2)**. Multivariate, cluster analysis is displayed for all five polarized MΦ phenotypes: M1 MΦs (IFN-γ/LPS treated, shown in red) **(A)**, M2a MΦs (IL-4/IL-13 treated, shown in yellow) **(B)**, M2b MΦs (IC/LPS treated, shown in green) **(C)**, M2c MΦs (IL-10 treated, shown in gray) **(D)**, and M2d MΦs (IL-6/LIF treated, shown in purple) **(E)**. Untargeted metabolomics profiles are based on three experimental replicates for each MΦ phenotype (N=3).

A.

1.

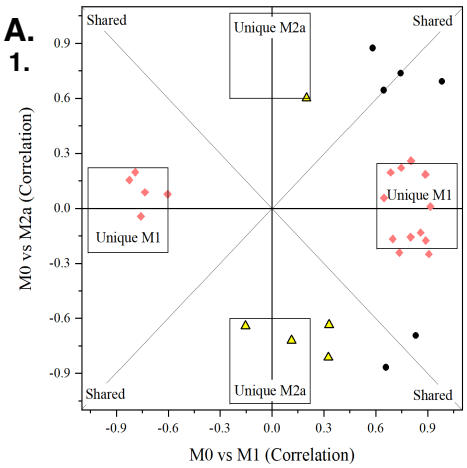

2.

Unique Metabolites	M1	M2a
kynurenine	0.93	-0.29
3-formylindole	0.92	0.01
itaconate	0.91	-0.25
N-formylanthranilic acid	0.89	-0.18
uracil	-0.04	-0.61
imidazole lactate	-0.15	-0.64
palmitoyl-myristoyl-glycerol	0.11	-0.72
N-stearoyl-sphingosine	0.33	-0.81
Shared Metabolites	**M1**	**M2a**
3-ureidopropionate	0.74	0.74
5-aminovalerate	0.58	0.87
N'1-acetylspermidine	0.66	-0.87
4-guanidinobutanoate	0.83	-0.69

3.

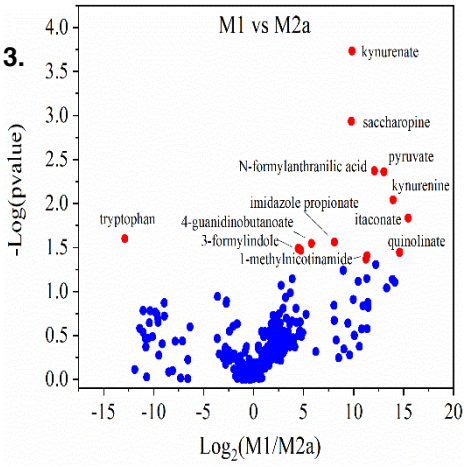

B.

1.

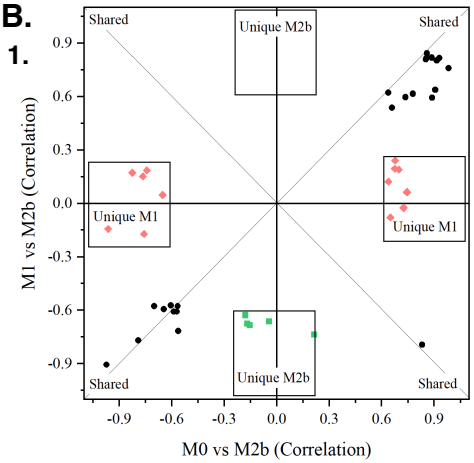

2.

Unique Metabolites	M1	M2b
3-ureidopropionate	0.74	0.06
N-acetylglutamine	0.70	0.19
nicotinamide	0.68	0.24
glycylleucine	-0.96	-0.14
uracil	-0.04	-0.66
N-stearoyl-sphingosine	0.33	-0.70
imidazole lactate	-0.15	-0.68
acetylcarnitine	-0.30	-0.83
Shared Metabolites	**M1**	**M2b**
kynurenine	0.93	0.82
quinolinate	0.85	0.81
itaconate	0.91	0.64
4-guanidinobutanoate	0.83	-0.79
tryptophan	-0.97	-0.91

3.

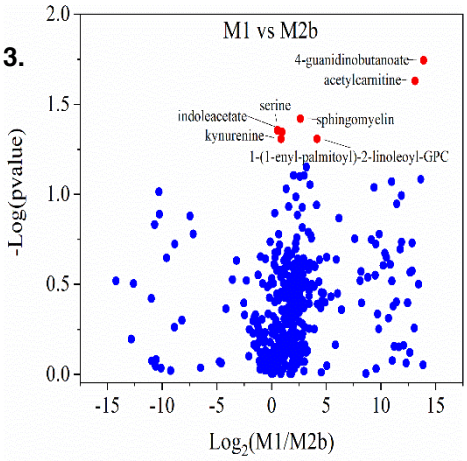

C

1.

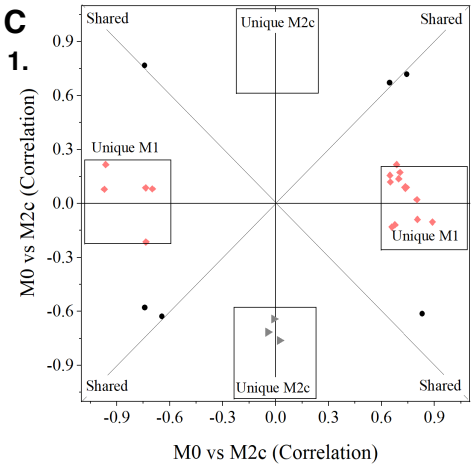

2.

Unique Metabolites	M1	M2c
tryptophan	-0.97	0.08
glycylleucine	-0.96	0.22
N-formylanthranilic acid	0.89	-0.10
3-hydroxy-3-methylglutarate	0.80	0.02
phenylpyruvate	0.80	-0.09
1-stearoyl-2-oleoyl-GPS	-0.01	-0.64
uracil	-0.04	-0.72
cysteine	0.02	-0.76
Shared Metabolites	**M1**	**M2c**
3-phosphoglycerate	-0.64	-0.63
3-ureidopropionate	0.74	0.72
4-guanidinobutanoate	0.83	-0.61
cysteinylglycine disulfide	-0.74	-0.58

3.

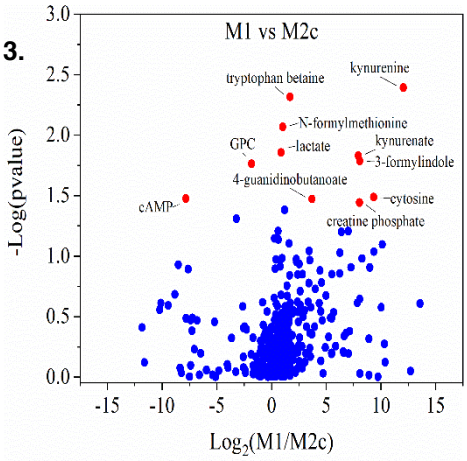

D

1.

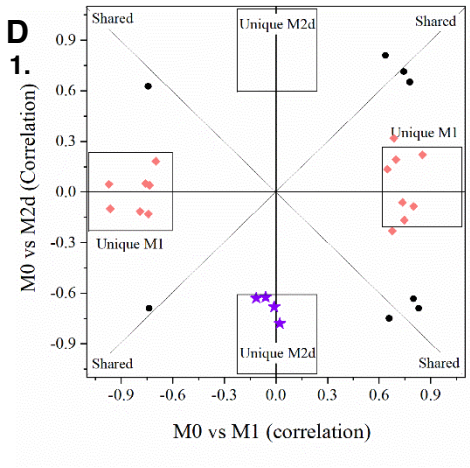

2.

Unique Metabolites	M1	M2d
glycerophosphoinositol	0.89	-0.28
quinolinate	0.85	0.22
glycylleucine	-0.96	-0.10
tryptophan	-0.97	0.05
cysteine	0.02	-0.78
1-stearoyl-2-oleoyl-GPS	-0.01	-0.68
3-hydroxyoctanoate	-0.06	-0.62
1-stearoyl-2-linoleoyl-GPS	-0.11	-0.63
Shared Metabolites	**M1**	**M2d**
imidazole propionate	0.78	0.65
3-ureidopropionate	0.74	0.71
prolylglycine	0.64	0.81
4-guanidinobutanoate	0.83	-0.69

3.

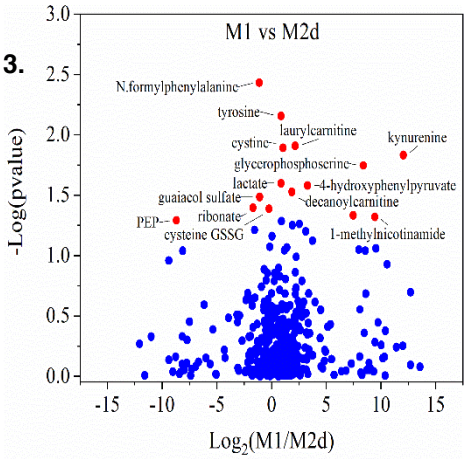

Figure 6: Global Metabolomics Comparison of the Classically-Activated Macrophage Phenotype (M1 MΦ) to Four Subtypes of Alternately-Activated Macrophage Phenotypes (M2a, M2b, M2c, & M2d MΦ). OPLS-DA clustering relative to the parent, resting MΦ phenotype (M0 MΦ) identified metabolite biomarkers correlated with all five polarized MΦ phenotypes based on OPLS-DA variable influence on projection (VIP) values. VIP values were used to identified both shared and unique metabolite biomarkers of the classically-activated M1 MΦ phenotype and four subtypes of the alternately-activated M2 MΦ phenotypes, displayed as OPLS-DA Shared and Unique Structures (SUS) plots (A.1, B.1, C.1, and D.1). For each SUS plot, metabolite biomarkers uniquely correlated to the M1 MΦ phenotype (red diamonds) are plotted along the x-axis and those metabolite biomarkers uniquely correlated to the M2 MΦ phenotype are plotted along the y-axis. Shared metabolite biomarkers (black circles) are plotted along the diagonals, reflecting biomarker positive/negative correlation to each polarized MΦ phenotype relative to the parent, resting MΦ phenotype (M0 MΦ). Associated biomarkers and correlation scores are shown in matching tables (A.2, B.2, C.2, and D.2). OPLS-DA SUS plots are displayed for four polarized M2 MΦ phenotypes, relative to the M1 MΦs (IFN-γ/LPS treated, shown in red): M2a MΦs (IL-4/IL-13 treated, shown in yellow) (A), M2b MΦs (IC/LPS treated, shown in green) (B), M2c MΦs (IL-10 treated, shown in gray) (C), and M2d MΦs (IL-6/LIF treated, shown in purple) (D). Untargeted metabolomics profiles are based on three experimental replicates for each MΦ phenotype (N=3).

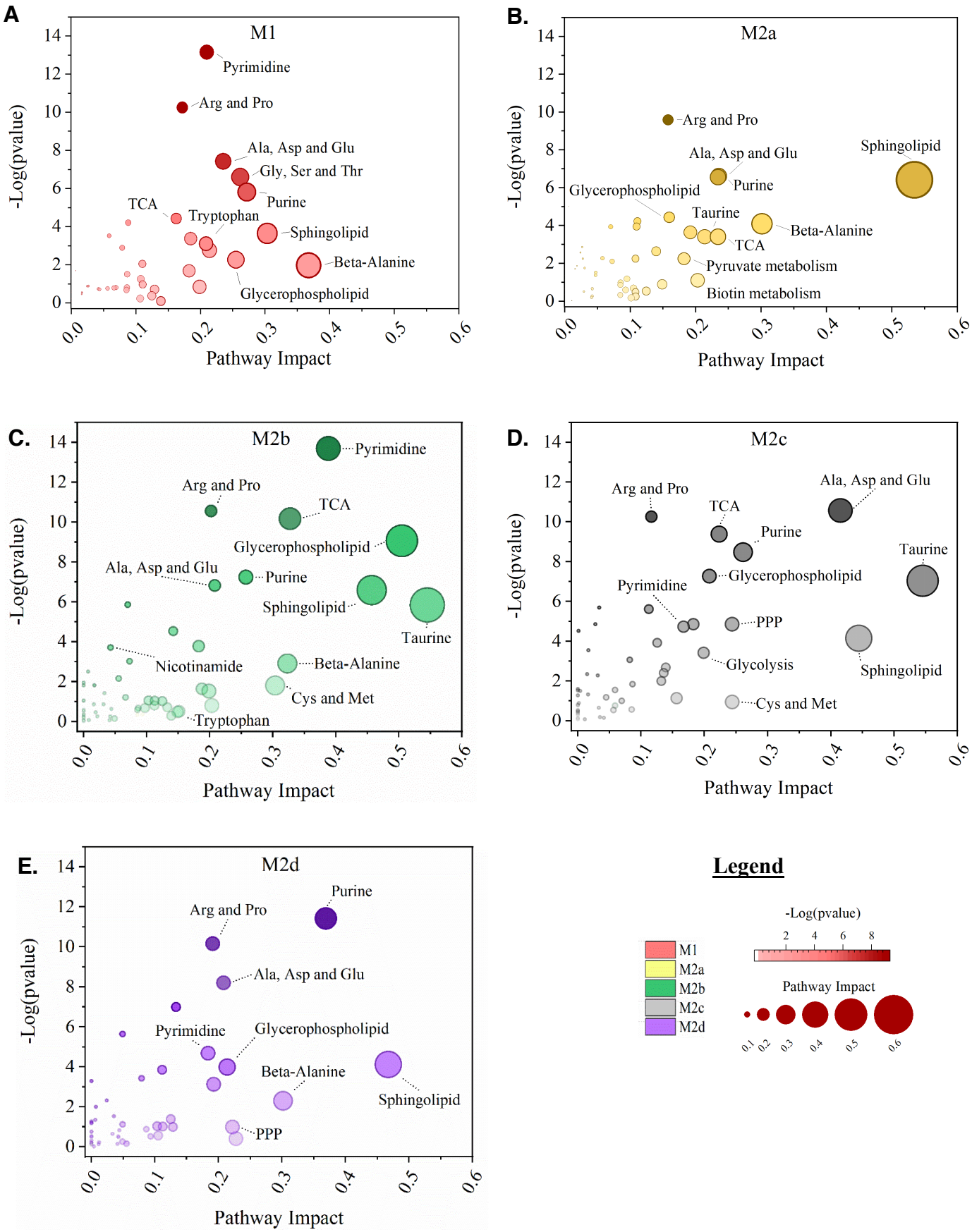
A
M1
Pyrimidine
Arg and Pro
Ala, Asp and Glu
Gly, Ser and Thr
Purine
TCA
Tryptophan
Sphingolipid
Beta-Alanine
Glycerophospholipid
-Log(pvalue)
Pathway Impact
B.
M2a
Arg and Pro
Ala, Asp and Glu
Purine
Sphingolipid
Glycerophospholipid
Taurine
Beta-Alanine
TCA
Pyruvate metabolism
Biotin metabolism
-Log(pvalue)
Pathway Impact
C.
M2b
Pyrimidine
Arg and Pro
TCA
Glycerophospholipid
Ala, Asp and Glu
Purine
Sphingolipid
Taurine
Nicotinamide
Beta-Alanine
Cys and Met
Tryptophan
-Log(pvalue)
Pathway Impact
D.
M2c
Arg and Pro
Ala, Asp and Glu
TCA
Purine
Taurine
Glycerophospholipid
Pyrimidine
PPP
Glycolysis
Sphingolipid
Cys and Met
-Log(pvalue)
Pathway Impact
E.
M2d
Purine
Arg and Pro
Ala, Asp and Glu
Pyrimidine
Glycerophospholipid
Beta-Alanine
Sphingolipid
PPP
-Log(pvalue)
Pathway Impact
Legend
M1
M2a
M2b
M2c
M2d
-Log(pvalue)
Pathway Impact

Figure 7: Metabotype Profiling of Polarized Macrophages. Untargeted, global metabolomics profile of polarized MΦ phenotypes identified 498 known compounds, normalized to total cell count, and profiled relative to the resting M0 MΦ phenotype. For normalized, M0-relative metabolite profiles, over-representation analysis by hypergeometric testing and pathway topology analysis by two node centrality measures (degree centrality and betweenness centrality) was performed for each polarized MΦ phenotype including M1 MΦs (IFN-γ/LPS treated, shown in red) (A), M2a MΦs (IL-4/IL-13 treated, shown in yellow) (B), M2b MΦs (IC/LPS treated, shown in green) (C), M2c MΦs (IL-10 treated, shown in gray) (D), and M2d MΦs (IL-6/LIF treated, shown in purple) (E). Metabolic Pathway Topology is plotted as Pathway Impact (x-axis) and significance of pathway topography (-Log [p value], y-axis) for each polarized MΦ phenotype.

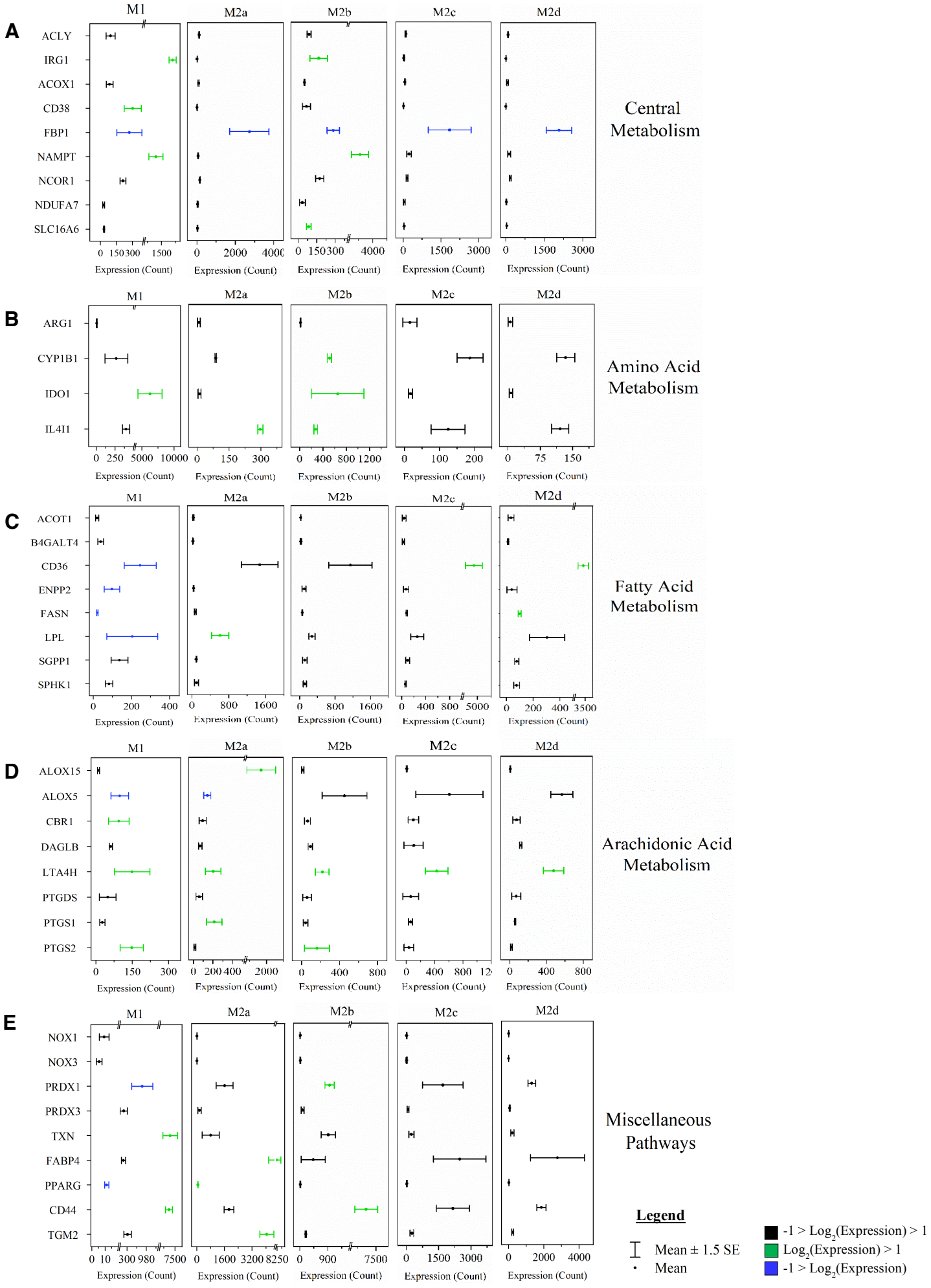
A
M1
M2a
M2b
M2c
M2d
ACLY
IRG1
ACOX1
CD38
FBP1
NAMPT
NCOR1
NDUFA7
SLC16A6
Expression (Count)
Central Metabolism
B
ARG1
CYP1B1
IDO1
IL4I1
Amino Acid Metabolism
C
ACOT1
B4GALT4
CD36
ENPP2
FASN
LPL
SGPP1
SPHK1
Fatty Acid Metabolism
D
ALOX15
ALOX5
CBR1
DAGLB
LTA4H
PTGDS
PTGS1
PTGS2
Arachidonic Acid Metabolism
E
NOX1
NOX3
PRDX1
PRDX3
TXN
FABP4
PPARG
CD44
TGM2
Miscellaneous Pathways
Legend
Mean ± 1.5 SE
Mean
-1 > Log2(Expression) > 1
Log2(Expression) > 1
-1 > Log2(Expression)

Figure 8: Macrophage Polarization into Functional Phenotypes Activates Distinct Metabolic Gene Expression Profiles Relative to the Parent, Resting Macrophage Phenotype (M0). Gene set enrichment analysis (GSEA) and pathway impact scoring of global myeloid gene expression demonstrates distinct patterns in metabolism-related transcripts in the five polarized MΦ phenotypes. Associated metabolism gene expression profiles for most impacted pathways are shown including A) central metabolism, B) amino acid metabolism, C) fatty acid metabolism, D) arachidonic acid metabolism, and E) miscellaneous pathways. Red bars represent gene targets that are differentially regulated ($p \leq 0.05$) when compared to the M0 phenotype. Myeloid gene expression was directly detected through molecular barcode probes and normalized to the geometric mean of the housekeeping gene set. Gene expression is mean ± SEM. Pathway topology and metabolic gene expression profiles are based on triplicate, experimental replicates (N=3).

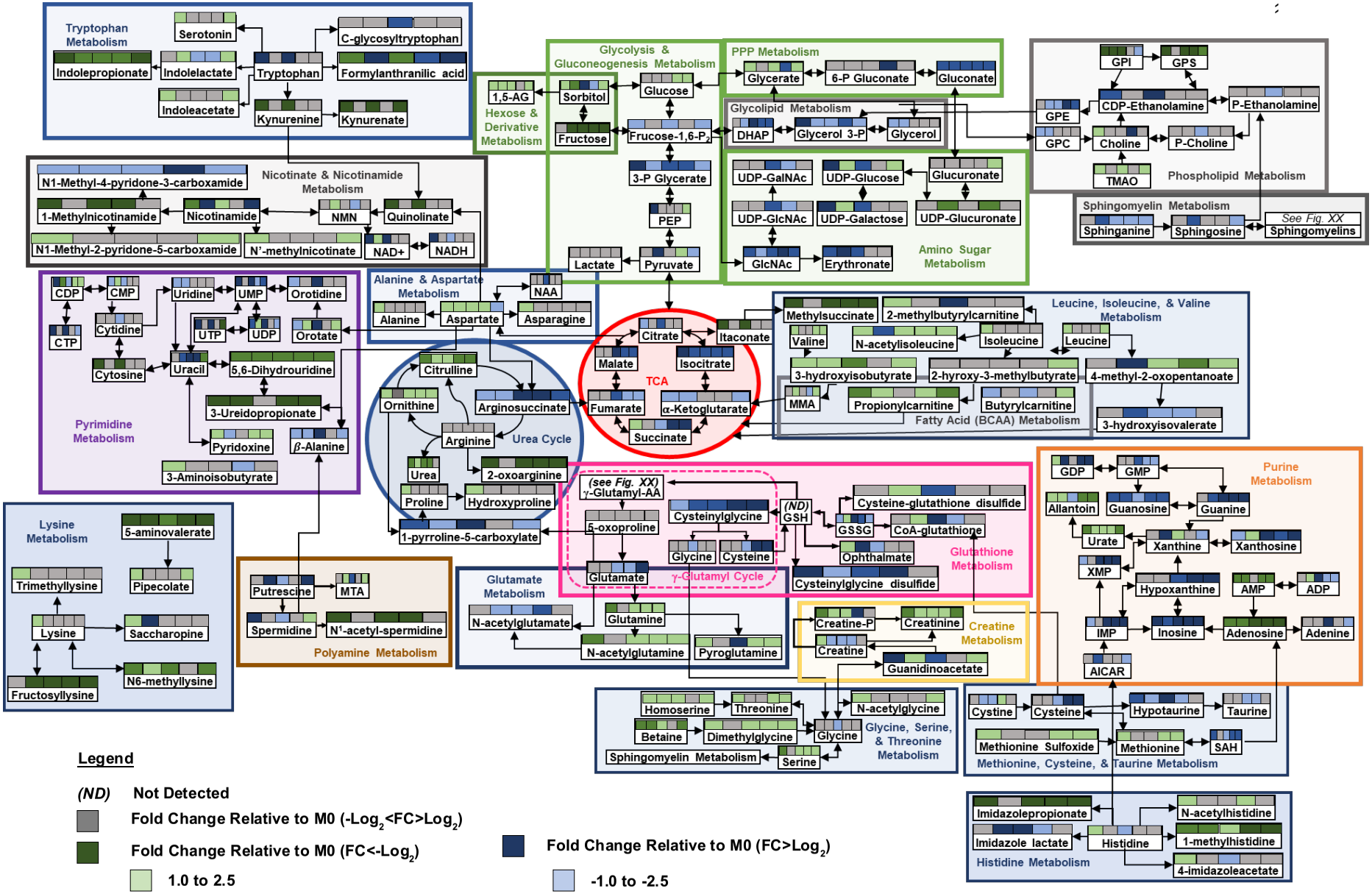

Legend

(ND) Not Detected

Fold Change Relative to M0 ($-Log_2$<FC>Log_2)

Fold Change Relative to M0 (FC<$-Log_2$)

- 1.0 to 2.5
- 2.5 to 5.0
- >5.0

Fold Change Relative to M0 (FC>Log_2)

- -1.0 to -2.5
- -2.5 to -5.0
- <-5.0